0203 DREV R 686/73
35 PROJ 97-01-19

NON CLASSIFIE
UNCLASSIFIED

04a ON THE PREDICTION OF CRATER PROFILES PRODUCED IN DUCTILE TARGETS BY THE IMPACT OF RIGID PENETRATORS AT BALLISTIC VELOCITIES

by

1101 P.N. Brooks

CENTRE DE RECHERCHES POUR LA DEFENSE
0204a DEFENCE RESEARCH ESTABLISHMENT
VALCARTIER,
0204b Valcartier QUE (CAN)
Tel: (418) 844-4271
Québec, Canada

46 January/janvier 1973

DC

RESUME

En se fondant sur une analogie aérodynamique impliquant une 'atmosphère' rigide-plastique, on a établi un modèle analytique de la pénétration et de la formation de cratères par des projectiles non-déformants dans des cibles ductiles. On a également déterminé une série de coefficients pouvant servir à la prédiction du comportement de projectiles à bout conique ou composés de deux sections coniques. Nos résultats concordent bien avec ceux obtenus expérimentalement et démontrent que le modèle peut servir à optimiser la conception d'un pénétrateur pour une gamme spécifique de vitesses et de matériaux.

ABSTRACT

The penetration and cratering process for non-deforming projectiles impacting ductile targets is modeled analytically on the basis of an aerodynamic analogy involving a rigid-plastic 'atmosphere'. A set of coefficients is determined which can be used to predict the behaviour of cylindrical projectiles having tips that are either purely conical or comprised of two conical sections. Comparisons made with experiment show good agreement for a variety of projectile/target combinations and demonstrate that the model can be used to optimize the design of a penetrator for a specific velocity range and target material.

TABLE OF CONTENTS

NOMENCLATURE

A_1	Cross-sectional area of conical tip.
A_2	Cross-sectional area of cylindrical body.
$A_3(x)$	Cross-sectional area at point of re-attachment.
A_c	Cross-sectional area of singly tapered penetrator.
$A_H(x)$	Cross-sectional area of crater at depth x.
C_β	Ballistic drag coefficient.
$C_{\beta 1}$	Ballistic drag coefficient associated with the conical tip.
$C_{\beta 2}$	Ballistic drag coefficient associated with the shoulder.
C_D	Profile drag coefficient.
d_c	Diameter of penetrator body.
d_t	Diameter of tip - doubly tapered projectile.
$\Delta E_H(x)$	Energy increment required to displace a volume of target material $A_H(x)\Delta x$
ΔE_c	Energy increment required to displace a volume of target material $A_c\Delta x$
ΔE_ρ	Kinetic energy increment given to a target layer of thickness Δx
E_o	Initial kinetic energy of the projectile.
K_2	Coefficient governing the rate of increase of flow stress with depth.
KE	Kinetic energy.
M	Penetrator mass.
N_B	Dimensionless number relating inertial forces to the flow stress. (Ballistic Number).
N_B^*	Value of N_B below which free hole expansion is elastic.
P_m	Maximum penetration, measured to shoulder.
r	Radial distance from axis of penetrator.
r	Radius of cylindrical body.
t	Time.
V(x)	Axial velocity.
V_o	Initial velocity
V_1	Axial velocity after conical tip is fully immersed.
$V_r(r,x)$	Idealized radial velocity distribution.
$V_r^*(r,x)$	True radial velocity distribution.
$V_{ro}(x)$	Radial velocity of target material at radius

Δv_c	Incremental penetrator volume. $A_c \Delta x$
v_f	Final crater volume.
x	Distance between free surface and shoulder.
x_1	Height of tip cone.
β_1	Tip angle of doubly tapered penetrator.
β_2	Shoulder angle of doubly tapered penetrator.
ρ	Density of target material.
$\tilde{\sigma}$	Average flow stress.
σ_c	Surface yield stress.
σ_{max}	Yield stress at infinite depth.

INTRODUCTION

The penetration of projectiles into metallic targets has been studied extensively for many years. In general, most researchers have attemped to develop theories that would allow the prediction of either the depth to which a projectile will penetrate, or the velocity at which it will completely perforate a given target, (Refs 1 - 6). It is recognized that the problem of predicting the behaviour of two bodies involved in high speed impact is extremely complex. The partition of the impact energy into, a) the plastic deformation of the two bodies, b) the formation of energetic fragments and c) the generation of heat and elastic waves, depends on the geometry of the bodies, the obliquity and velocity of the impact and most important, the equations of state for the two materials under the particular conditions of impact. Some attempts at the rigorous solution of this problem are currently being made with the aid of large computer codes. However, such is the complexity of the problem that current limitations in the capacity of todays computers restricts the class of impact problem to chose which exhibit axial symmetry i.e. the problem must be effectively two dimensional. Purely analytical attempts at penetration dynamics have in most cases been restricted in the same way. Generally, the problems which have been studied, have been limiting cases. The following examples are characteristic:

a) The hypervelocity impact of a sphere which is treated as a point source of energy.

b) The hypervelocity impact of a rod which is treated as a hydrodynamic jet.

c) The low speed impact of a non-deforming projectile which is assumed to make a hole of the same diameter as the projectile.

d) The impact of a flat ended cylinder against a thin plate which punches out a circular disc.

In all of the above cases, normal impact is assumed as well as some characteristic of the deformation process.

While it is true that in practice normal impact occurs very rarely, (except in the case of industrial processes), the study of these special cases has contributed enormously to the understanding of the more general impact problem. Certainly in most instances, the perforation of a target by a projectile involves two or more of the penetration modes which predominate in the examples given previously, eg. spherical cavity expansion, radial plastic flow or adiabatic shear.

The purpose of the present study is to extend the usual objective of predicting the depth of penetration, by also predicting the shape of the crater that will be formed by the impact of non-deforming

conically tipped projectiles. In practice, slender ogival projectiles (Figure 1a) will penetrate a ductile target without any hole enlargement due to lateral acceleration of the target material. This results in a highly efficient usage of the impact energy and maximizes the penetration. On the other hand, the slender ogive is not an efficient shape for the attack of oblique targets as ricochet is caused by an initial surface contact (rather than line or point contact) on impact. To overcome this effect, the tendency has been to use doubly-tapered conical penetrators (Figure 1b). We find however, that at high velocity, two other phenomena arise which degrade the ability of the projectile to penetrate. Firstly, the relatively blunt shape causes much higher stresses on impact which may cause shattering or plastic deformation of the penetrator, and secondly, if penetrator deformation does not occur, the large lateral inertia of the target material as it flows across a conical tip causes the formation of a crater whose diameter is larger than that of the penetrator itself. The energy of the impact is directly related to the crater volume hence any increase in diameter implies a reduction in the maximum penetration. The object of this study is to relate the crater profile to the projectile geometry and thus permit the selection of conically blunted nose shape which will, for a given impact velocity, produce a uniform crater of the same diameter of the penetrator.

ANALYSIS

Let us first consider a rigid projectile penetrating a homogeneous isotropic semi-infinite target. Let the target material have a density ρ and an average plastic flow stress σ. Depending on the axial velocity $V(x)$, the average target flow stress $\tilde{\sigma}$ and the shape of the penetrator, the target material may or may not separate from the shoulder of the projectile. Five possibilities are shown in Figure 2 to illustrate the effect of shape on the resulting profile. In case (a), the ogival profile produces lateral acceleration of the target material that diminishes smoothly to zero at the shoulder. The result is that the 'flow' of plate material remains 'attached' and the crater cross-section is the same as that of the penetrator. In case (b) the conical tip produces high lateral acceleration at the shoulder and imparts more kinetic energy to the target material than can be stored elastically. The result is that the target flow separates at the shoulder and produces a crater cross-section greater than that of the penetrator. In case (c), the penetrator has a doubly-tapered profile and is penetrating at a velocity that is high enough to cause separation at the first shoulder and produce a crater cross-section greater than that of the penetrator. In case (d), the penetrator is of the same profile as in case (c), but the penetration velocity is lower. Once again the flow separates at the first shoulder but is not sufficiently energetic to produce a crater cross-section greater than that of the penetrator. As a result, the flow impinges on the second taper, is accelerated a second time and then finally separates from the rear shoulder. Finally in case (e), we

have a combination of cases (a) and (d). The profile is a conically tipped ogive which causes separation at the front shoulder. Here again the flow is not energetic enough to produce a crater diameter greater than that of the penetrator. However in this case the flow reattaches on the ogival surface which produces an acceleration that diminishes to zero at the rear shoulder and allows the flow to remain attached. It should be noted that the ogival profile will only produce attached flow if the ogive radius is made sufficiently large for a given V(x) and $\tilde{\sigma}$. If the curvature is too small, then separation can occur.

Let us now assume that the projectile shape is such that the target material does separate from the shoulder i.e. that target inertia effects are of the same magnitude as the dynamic flow stress. If we wish to describe the motion of this projectile, the similarity between the penetrating projectile and a projectile flying through a fluid medium immediately suggests an equation of the form:

$$M\ddot{X} = -\sigma A_c - \tfrac{1}{2}\rho C_D A_c V^2(x), \tag{1}$$

where M is the projectile mass
A_c is the cross-sectional area of the penetrator
and C_D Is the 'profile' drag coefficient which depends only on the projectile and perhaps the Mach number.

A second analogy which suggests itself is that of an equivalent non-separating penetrator whose cross section varies with the depth of penetration in the same manner as the crater profile. We would then simply write:

$$M\ddot{X} = -\tilde{\sigma}A_H(x) \tag{2}$$

From experiment, we know that the total kinetic energy of impact is closely proportional to the final hole volume and that the constant of proportionality is the average dynamic flow stress, i.e.,

$$E_o = \tilde{\sigma}v_f$$

where E_o is the initial kinetic energy of the penetrator and v_f is the final crater volume. Consider now a displacement Δx of the projectile shown in Figure 3. A known amount of energy ΔE_c will have been used to displace the volume occupied by the projectile, i.e.

$$\Delta E_c = \tilde{\sigma}\Delta v_c = \tilde{\sigma}A_c\Delta x \tag{3}$$

The total increment of energy ΔE_H is unknown because the final area $A_H(x)$ is unknown. We may write:

$$\Delta E_H = \tilde{\sigma} A_H(x) \Delta x. \tag{4}$$

Also,

$$(\Delta E_H)_{max} = \Delta E_c + \Delta E_p, \tag{4'}$$

where ΔE_p is the total kinetic energy increment given to the complete layer Δx at the point of separation.

The energy ΔE_p may be calculated if the radial velocity gradient is known. In the sequence shown in Figure 2, it is assumed that there is no shear interaction between layers and that all target motion is radial. The sequence of events in as follows:

a) The projectile is at position x, moving with velocity V(x)

b) The projectile has traveled to position x + Δx, slowed to velocity V(x + Δx) and imparted a radial velocity $V_{ro}(x + \Delta x)$ to the interface of the disc Δx.

c) The disc Δx has moved laterally and is slowing down as its energy is dissipated by doing work against $\tilde{\sigma}$

d) Lateral motion is complete

If we assume that the target material is incompressible and that there is no axial motion, the equation of continuity states that the radial velocity distribution in the layer Δx at the start of lateral motion is,

$$V_r(x,r) = (r/r_o)V_{ro} \tag{5}$$

However, this conclusion is physically unacceptable, as it leads to an infinite energy in each layer. It is clear that boundary displacements and compressibility will, in practice, combine to produce a bounded velocity distribution, $V_r^*(r,x)$ as shown in Figure 4. At the present time these effects cannot be specified hence the function $V_r^*(r,x)$ is also unknown.

For the kinetic energy of the layer Δx at the start of lateral motion, we may write:

$$\Delta E_p(x) = \int_{r_o}^{\infty} dE_p(r,x),$$

where $$dE_p(r,x) = \tfrac{1}{2}(2\pi r)dr\Delta x\rho V_r^{*2}(r,x),$$

the energy of an elemental ring at radius r. Then

$$\Delta E_p(x) = \pi\Delta x\rho V_{ro}^2(x)\int_{r_o}^{\infty} r((V_r^{*2}(r,x))/(V_{ro}(x)))dr$$

or $$\Delta E_p(x) = \pi\Delta x\rho V_{ro}^2(x)r_o^2\int_1^{\infty}(r/r_o)(V_r^*/V_{ro})^2 d(r/r_o) \qquad (6)$$

Referring to Figure 5, we may express the radial velocity V_{ro} as a function of the axial penetrator velocity, i.e.,

$$V_{ro}(x) = (\text{Sin}\beta\ \text{Cos}\beta)V(x)$$

This equation assumes that penetration velocities are sufficiently high to produce a condition of adiabatic shear on the conical interface and effectively eliminate friction, (Ref. 3). In other words the absolute motion of the target material that is in contact with the conical tip is normal to the interface.

Velocities of interest in this study are considerably lower than elastic wave velocities in the target, hence wave phenomena will be unimportant. This suggests that the magnitude of the true radial velocity at any radius will be directly proportional to the axial velocity V(x), and we would therefore expect that normalizing this distribution with respect to V_{ro} would result in a function of $\frac{r}{r_o}$ and β only. This function would probably be in the form of a product of two separable functions of $\frac{r}{r_o}$ and β. For a given depth x, let

$$(V_r^*/V_{ro}) = f(r/r_o,\beta)$$

Then we may write:

$$\Delta E_p(x) = \pi r_o^2 \Delta x \rho \sin^2 \cos^2 \beta V^2(x) \int_1^\infty (r/r_o) f(r/r_o, \beta) d(r/r_o)$$

Let $$2\sin^2\beta\cos^2\beta \int_1^\infty f(r/r_o, \beta)(r/r_o) d(r/r_o) = C_\beta$$

a function of β only.

Then $$\Delta E_p(x) = \tfrac{1}{2} A_c \Delta x \rho V^2(x) C_\beta \tag{7}$$

returning now to equations (4) and (4')

$$(\Delta E_H(x))_{max} = \Delta E_c + \tfrac{1}{2} A_c \Delta x \rho V^2(x) C_\beta = \tilde{\sigma} A_H \Delta x$$

or $$A_H(x) = (\Delta E_c + \tfrac{1}{2} A_c \Delta x \rho V^2(x) C\beta)/\tilde{\sigma}\Delta x$$

From (3) $$A_H(x) = (\tilde{\sigma} A_c \Delta x + \tfrac{1}{2} A_c \Delta x \rho V^2(x) C_\beta)/\tilde{\sigma}\Delta x$$

$$A_H(x) = A_c + (\tfrac{1}{2}\rho A_c C_\beta V^2(x))/\tilde{\sigma}. \tag{8}$$

Let $$N_B = \tfrac{1}{2}\rho V^2(x)/\tilde{\sigma}$$

then $$A_H(x) = A_c(1+N_B C_\beta). \tag{9}$$

N_B is simply a dimensionless number formed by the ratio of the dynamic inertial pressure in the target material and the local material flow strength. It is similar in character to the Reynolds number (a ratio of inertial to viscous forces) as used in fluid mechanics, except that in this case, the penetrator is moving through a medium whose elastic cohesion greatly exceeds forces which are dependent on viscous effects. N_B will, for convenience, be referred to as the ballistic number.

From equation (2) and (8), we obtain:

$$M\ddot{X} = -\tilde{\sigma}A_c - \tfrac{1}{2}\rho A_c C_\beta V^2(x), \tag{10}$$

where

$$C_\beta = 2\mathrm{Sin}^2\beta\mathrm{Cos}^2\beta \int_1^\infty f(\beta)\, \xi\, d\xi$$

a function of the projectile shape only. Equation (10) which is exactly the same as Equation (1), gives support to the use of an aerodynamic analogy and at the same time indicates the assumptions involved in the use of such an analogy. Equation (10) may be written,

$$MV\frac{dV}{dx} = -A_c\left(\tilde{\sigma} + \tfrac{1}{2}\rho C_\beta V^2(x)\right)$$

which may be integrated directly to give

$$(x-x_1) = \frac{M}{\rho A_c C_\beta}\left[\mathrm{Log}\left\{\frac{\tfrac{1}{2}\rho C_\beta V_1^2 + \tilde{\sigma}}{\tfrac{1}{2}\rho C_\beta V^2 + \tilde{\sigma}}\right\}\right] \tag{11}$$

where V_1 is the velocity when the shoulder of the penetrator is first immersed in the target, i.e. the point of the penetrator has moved a distance x_1 into the target. Equation (11) yields V(x) explicitly:

$$V(x) = \left[\frac{2}{\rho C_\beta}\left\{\left[\frac{\tfrac{1}{2}\rho C_\beta V_1^2 + \sigma}{\exp\left\{\frac{\rho A_c C_\beta (x-x_1)}{M}\right\}}\right] - \sigma\right\}\right]^{\frac{1}{2}} \tag{12}$$

or

$$V(x) = \left[\frac{2\sigma}{\rho C_\beta}\left\{\left[\frac{N_{B1}C_\beta + 1}{\exp\left\{\frac{\rho A_c C_\beta (x-x_1)}{M}\right\}}\right] - 1\right\}\right]^{\frac{1}{2}}. \tag{13}$$

Combining equations (8) and (12), we obtain:

$$A_H(x) = A_c\left[1 + \frac{1}{\sigma}\left\{\left[\frac{\tfrac{1}{2}\rho C_\beta V_1^2 + \tilde{\sigma}}{\exp\left(\frac{\rho A_c C_\beta (x-x_1)}{M}\right)}\right] - \tilde{\sigma}\right\}\right]$$

or,

$$A_H(x) = A_c\left\{\frac{N_{B1}C_\beta + 1}{\exp\left(\frac{\rho A_c C_\beta (x-x_1)}{M}\right)}\right\} \tag{14}$$

Equation (14) defines the hole profile explicitly in terms of the position x and indicates that for a given target density the hole profile is invariant for a given penetrator if the initial ballistic number is matched.

Variable Target Resistance

In the ballistic model presented thus far, it has been assumed that the penetration process starts with the conical tip of the penetrator immersed in the target material and that the penetrator encounters the same plastic resistance at all depths. The model will now be further refined to accomodate the entry phase, a variation of flow stress with depth, an elastic limit below which permanent hole enlargement does not occur and penetrators with doubly-tapered tips.

During the immersion of the conical tip, geometric similarity prevails, i.e. the vertical component of stress acting on the tip does not vary with depth but remains constant at some value σ_c which will depend on the angle of the cone. The energy lost by the projectile during this phase will be directly proportional to the volume displaced, the constant of proportionality being the flow stress σ_c, i.e.,

$$\Delta KE = (\tfrac{1}{3}\pi r_o^3 \mathrm{Cot}\beta)\sigma_c \ . \qquad (15)$$

Hence the remaining energy after nose immersion is,

$$KE_1 = KE_o - \Delta KE$$

$$= \tfrac{1}{2}MV_o^2 - (\tfrac{1}{3}\pi r_o^3 \mathrm{Cot}\beta)\sigma_c .$$

The initial velocity of entry of the cylindrical body is then

$$V_1 = \left\{(\tfrac{1}{2}MV_o^2 - \tfrac{1}{3}\sigma_c \pi r_o^3 \mathrm{Cot}\beta)/\tfrac{1}{2}M\right\}^{\frac{1}{2}}$$

or

$$V_1 = \left\{V_o^2 - (2\sigma_c/3M)\pi r_o^3 \mathrm{Cot}\beta\right\}^{\frac{1}{2}} \qquad (16)$$

After the immersion of the conical tip is completed, the flow stress of the target material should increase with depth in the manner associated with static punching. As the depth increases, the distortion zone surrounding the penetrator moves away from the free surface of the target, the constraint becomes more severe and at great depth (in a target of semi-infinite extent) the stress state becomes hydrostatic. Thus we must anticipate that the flow stress will initially be σ_c and will increase and asymptotically approach some maximum stress σ_{max} which will depend on the fundamental characteristics of the target material.

The variation of stress with depth (as observed in static punching experiments) may be suitably approximated by an equation of the form,

$$\sigma_x = \sigma_{max} - (\sigma_{max} - \sigma_c)\exp-(K_2 x/d_c) \tag{17}$$

or $$\sigma(x) = \sigma_{max}(1 - (1 - (\sigma_c/\sigma_{max}))\exp-(K_2 x/d_c)) \tag{18}$$

It should therefore be possible to use one target material to determine the variation of the ratio σ_c/σ_{max} with cone angle and so determine $\sigma(x)$ for any other values of σ_{max} (a second target material) or β.

As the shoulder of the penetrator enters the target, material is displaced laterally at some velocity V_{ro}, thus producing a crater of greater diameter than that of the penetrator itself. It is to be expected that some limiting velocity V_{ro}* will exist below which no permanent enlargement of the hole will result, i.e., an elastic limit is reached at which the kinetic energy imparted to the plate material as it is accelerated laterally by the conical shoulder can be stored as elastic strain. In the earlier development of the aerodynamic analogy, no assumption was made with regard to the constancy of $\sigma(x)$, (except on an incremental basis) in obtaining equation (8), hence this equation remains valid for a target strength which is functionally dependent on the penetration depth. We may readily modify this equation to include an elastic limit, i.e., for a given target material, we simply postulate a minimum value for the ballistic number which will at all depths be subtracted from the current value of $N_B C\beta$. Equation (8) then becomes

$$A_H(x) = A_c(1 + N_B C_\beta - N_B^*), \quad N_B C_\beta > N_B^* \tag{19}$$

$$A_H(x) = A_c, \qquad N_B C_\beta \leq N_B^*,$$

where N_B* is the minimum value of the ballistic number at which hole areas greater than A_c will occur. It should be noted that the stress $\sigma(x)$ is an average stress acting on the nose of the penetrator. If the stress was in fact constant we would expect the limiting ratio N_B* (if based on the radial velocity of the target material) to be equal to unity. In other words, no permanent expansion would occur if the local flow stress exceeded the dynamic pressure of the target material as it left the shoulder. However, it is more reasonable to postulate a distribution of stress around the nose having a maximum value on the axis and varying with azimuth angle to a minimum at the shoulder. A directionally dependent yield stress (as seen by the contact surface) is compatible with the distribution of plastically deformed and perhaps work hardened material, (Figure 6). We may therefore expect that N_B* will be less than unity.

As obtained previously, the equation of motion of the penetrator is

$$\frac{MVdV(x)}{dx} = -\sigma(x)A_c - \tfrac{1}{2}\rho A_c C_\beta V^2(x)$$

where $\sigma(x)$ is now functionally related to the instantaneous depth of penetration. The coefficient C_β is still a function of the shape only. If $\sigma(x)$ is known, the difference equation

$$\Delta V = -((\sigma(x) + \tfrac{1}{2}\rho C_\beta V^2(x))A_c \Delta x)/MV(x) \qquad (20)$$

may be integrated numerically from $x_1<x<x_{max}$ and from $V_1<V(x)<o$. Knowing the variation of velocity with depth, we may evaluate $N_B(x)$ and so obtain the hole area variation $A_H(x)$ from equation (19).

Doubly Tapered Penetrators

Let us now consider the effect of having a doubly-tapered penetrator as shown in Figure 7. As before, we may use equations (19) and (20) to calculate $V(x)$ and $A_H(x)$ simply by making the following substitutions:

$$A_c \longrightarrow A_1$$
$$r_o \longrightarrow r_1$$
$$C_\beta \longrightarrow C_{\beta 1}$$

When the velocity of the penetrator drops to the level at which the crater area is just equal to the penetrator area, the equation of motion must be changed. As penetration progresses, the separated flow of plate material from the tip cone will re-attach on the shoulder cone and once again receive a lateral acceleration. If this secondary acceleration is sufficiently strong, re-separation will occur at the shoulder and hole enlargement will begin again.

This sequence is shown in Figure 7.

When $A_{H1}(x)<A_2$, we must write,

$$\frac{MVdV}{dx} = -A_1\left[\sigma_1(x) + \tfrac{1}{2}\rho V^2 C_{\beta 1}\right] - (A_2 - A_3)\left[\sigma_2(x) + \tfrac{1}{2}\rho V^2 C_{\beta 2}\right], \qquad (21)$$

where $\sigma_1(x)$ and $\sigma_2(x)$ are the characteristic flow stresses associated with linear cones with angles β_1 and β_2 respectively. The area A_3 is simply

$$A_3 = A_1(1 + N_{B1}C_{\beta 1} - N_B^*)$$

From (21) we get the difference equation

$$\Delta V = -\Delta x \left\{ A_1\sigma_1(1 + N_{B1}C_{\beta 1}) - A_1\sigma_2(1 + N_{B1}C_{\beta 1} - N_B^*) \right. \\ \left. (1 + N_{B2}C_{\beta 2}) + A_2\sigma_2(1 + N_{B2}C_{\beta 2}) \right\} / MV \qquad (22)$$

Equation 22 describes the variation of velocity with depth of a doubly-tapered penetrator as shown in Figure 8, condition (c). The hole area variation corresponding to equation (22) is simply:

$$A_H(x) = A_2 + (A_2 - A_3)(N_{B2}C_{\beta 2} - N_B^*)$$

Substituting for A_3, we obtain:

$$A_H = A_2(1 + N_{B2}C_{\beta 2} - N_B^*) - A_1(1 + N_{B1}C_{\beta 1} - N_B^*)(N_{B2}C_{\beta 2} - N_B^*) \qquad (23)$$

A step by step sequence showing the formation of a crater is given schematically in Figure 9. The preceeding equations have been programmed in APL to handle singly or doubly-tapered penetrators with separation occurring either at the front or rear shoulder. A listing of this program and a sample solution are given in Appendix A.

EXPERIMENT

A series of ballistic impacts were performed by firing hard non-deforming projectiles into semi-infinite ductile targets. A 0.57 inch smooth bore gun was used to launch the projectiles which were permitted a free flight of thirty inches prior to impact. The short flight was necessary to ensure a minimum of projectile yaw. Projectile velocities were measured by means of a disturbed magnetic field technique with an accuracy of 0.07% (Ref. 7) and, immediately prior to impact, the attitude of the projectile was monitored by orthogonal flash-radiography. A typical radiograph is shown in Figure 10.

The following specific experiments were carried out to investigate the usefulness of the proceeding analysis.

1) A series of 0.4 inch diameter hard steel projectiles with semi-apical angles from 10° to 90° were fired into soft aluminum targets to provide data for the determination of the coefficients C_β and K_2 as functions of β, the variation of the ratio σ_c/σ_{max} as a function of β, and the value of the critical ballistic number N_B^*.

   A typical projectile in this series (Figure 11), consisted simply of the hard steel penetrator and a light plastic sabot. Comparisons made between the craters of projectiles

with discarding and non-discarding sabots showed that the sabot caused no measurable change in the deformation. Non-discarding sabots, which are considerably cheaper to manufacture, were therefore used throughout the study. The targets consisted of four inch diameter cylinders of annealed 65-S Aluminum six inches in length, (Table I, Type 1). All of the targets used in this experiment were taken from the same lot of aluminum stock and heat treated simultaneously to ensure uniformity. An attempt was made to fire all the projectiles at the same velocity (2500 ft/s) by using the identical propellant charge weights. However, round to round variations gave a spread in velocity from 2430 to 2600 ft/s as shown in Table II.

2) The above experiment was repeated at somewhat lower impact velocities (Table III) to determine how effectively the computer simulation could predict the influence of a velocity change on crater profile and depth of penetration. No other parameters were changed.

3) A series of tungsten carbide projectiles with 30° semi-apical angle were fired into mild steel targets (Table I Type 2) at velocities from 1653 ft/s to 2985 ft/s to obtain data on the effect of a change of both projectile density and target material (Table IV).

4) The above experiment (No. 3) was repeated with harder steel targets (Table I Type 3) over a somewhat wider range of velocities, i.e. 1900 to 3900 ft/s, (Table V).

5) In the final experiment, a set of doubly-tapered steel projectiles having semi-apical angles of 60° and 10°, were fired into the Type 1 targets at velocities of roughly 2000 and 2500 ft/s (Table VI). Six different tip diameters were used as indicated in Figure 12. The object of this experiment was to determine whether or not a doubly-tapered projectile could be designed to produce a hole of uniform diameter equal to that of the projectile. Further, to compare the results with computer simulations made with the coefficients determined in the first experiment and if successful, to provide support for the original hypothesis.

RESULTS

From the analysis described earlier, a set of equations (14,19 and 20) were developed from which a prediction could be made of the crater profile and depth of penetration resulting from the impact of a non-deforming conical penetrator on a ductile target.

Contained in these equations were the following parameters:

C_β, a 'drag' coefficient, dependent only on the shape of the projectile and directly proportional to the instantaneous inertial resistance experienced by the projectile at a given velocity,

σ_c, the vertical component of flow stress acting on the tip of the projectile at the surface of the target, dependent on both the shape of the projectile and the physical characteristics of the target material,

σ_{max}, the maximum flow stress felt by the tip of the projectile at large depth, dependent only on the physical characteristics of the target material,

K_2, an exponent controling the rate of increase in flow stress acting on the projectile with increasing depth, dependent only on the shape of the projectile, and

N_B^*, a limiting value of the ballistic number below which hole enlargement will not occur, independent of the shape of the projectile or the type of target material and depending only on the mode of deformation, i.e. is the hole being generated by radial plastic flow?

For a given impact, these five parameters must be specified in order to define the hole profile in terms of:

1) the hole diameter at the surface,

2) the depth at which the hole diameter becomes the same as that of the projectile,

3) the curvature of the profile where the diameter exceeds that of the projectile, and

4) the total depth of penetration.

At first glance, it might appear that the use of five parameters may, in effect, be over-defining the problem. However, the following points should be noted:

1) these five parameters must also contend with changes in impact velocity and in the density of either (or both) the projectile or target materials.

2) the parameter N_B^* is a constant for the mode of deformation under consideration regardless of projectile shape or target material, and

3) the parameters C_β, K_2 and the ratio σ_c/σ_{max} are all functions of β only and once determined for a given projectile/target interaction, must be applicable for all other combinations that produce the same deformation mode.

Experiment No. 1

This experiment was set up specifically to provide a series of crater profiles that would allow the determination of the above parameters. Initially, a series of crater profiles were computed with arbitrarily chosen values of the parameters to give some insight into how the profile responded to changes in any specific parameter. An experimental profile was then selected and all the parameters varied systematically until a good match was obtained based on the four criteria mentioned previously. Having established an approximate level for each parameter, two new cone angles were selected on either side of the first and the process repeated, starting with the values obtained for the first profile. If it was not possible to obtain a good match, (i.e. σ_{max} and N_B^* were both fixed by the first profile) it was then necessary to return to the first profile and change the values of C_β and/or N_B^*. Successive iterations were performed until a good match was obtained for three adjacent values of β. At this point, the coefficients were plotted as functions of β to provide a gradient for estimating appropriate values for new cone angles. This process was continued until all the profiles from 15° to 90° were approximated and smooth functional distributions were obtained for C_β, K_2 and σ_c. The simulations obtained by this process are compared with the experimental profiles in Figure 13 to 28 together with radiographs of the actual craters. The depths of penetration are compared numerically in Table II. No simulation was made for $\beta = 10°$ because in all cases, the point of the projectile was destroyed during the penetration, (Figure 29). The final distributions of σ_c/σ_{max}, C_β and K_2 are presented in Table VII and shown graphically in Figures 30, 31 and 32. The variation of flow stress with depth has been calculated and is given in non-dimensional form in Figure 33.

In general, the profile matching yielded good results insofar as the general shape, point of re-attachment and total depth were concerned. Clearly however, for values of $\beta > 20°$, the crater diameter does not decrease in the uniform manner predicted by the simulation. The rate of change of diameter is certainly not a monotonic function of the depth and it would require a much more complex flow stress function to simulate the true variation. On the other hand the coefficient distributions are well behaved and physically acceptable. The ratio of σ_c/σ_m extrapolates to zero with β and tends asymptotically to unity as β approaches 90°. This is supported by static measurements made of the deformation ahead of conical punches which indicate a high degree of similarity in the target distortion for half-angles in excess

of 60° (Ref. 8). Figure 34 shows the deformation fields associated with a series of conical penetrators pressed slowly into laminated clay targets. It can be seen that up to $\beta = 50°$, there is evidence of the projectile point cutting through the layers. At $\beta = 90°$ the punch has formed a cap with a half-angle of roughly 55°. It is not surprising then to find in the range $60 < \beta < 90°$ that the ratio σ_c/σ_{max} only varies from 0.92 to 1.0. It is also of interest to note for $\beta = 90°$, that a constant flow stress gave the best profile match.

As might be expected, the drag coefficient C_β is zero for $\beta = o$ and increases monotonically with β to a maximum of 1.5 at $\beta = 90°$. The exponent K_2, which controls the rate of increase of stress with depth, was itself found to vary exponentially with the semi-apical angle β, i.e..

$$K_2 = 1.6e^{-.0381\beta},$$

where β is expressed in degrees.

Of the remaining two parameters, N_B^* is the most interesting in that a value of 0.5 gave the best results. One is immediately tempted to look for some simple relevance to account for this familiar fraction. However, in the authors opinion, it is more likely to be a result of the assumptions made in formulating this model than evidence say of a basic physical relationship between the local flow stress at the shoulder and that at the stagnation point. Finally, the maximum flow stress σ_{max} was estimated at a value of 87500 lb in^{-2}. This is approximately five times the value of the conventional ultimate tensile strength, (Table I).

Experiment No. 2

The coefficients determined in the above experiment were next used to calculate profiles for the same set of projectiles impacting the Type 1 target, this time at velocities of the order of 2100 ft/s. The results of this experiment are again given in Figures 13-28 which show radiographs of the craters and a direct comparison between the experimental profile and the computer simulation. Table III shows the difference between the computed and measured depths of penetration. Comparison of the experimental profiles with those obtained in the first experiment indicates that as β increases, there is less dependence of the initial crater diameter on the impact velocity. As before, the rate of change of profile diameter is not monotonic for $\beta > 20°$. Although the computed profiles do not reproduce the experimental variation in diameter, they do give a good approximation, particularly with respect to the point of re-attachment. As seen in Table III, the computed penetration is generally higher than the experiment by amounts ranging up to 9.3%.

Experiment No. 3

This experiment was selected to determine the predictive capability of the simulation with respect to changes in target material and in projectile mass and density. Tungsten carbide singly-tapered penetrators ($\beta = 30°$), were fired into mild steel targets at velocities from 1650 to 2985 ft/s. Radiographs of the craters are shown in Figure 35, and a comparison between experimental and computed profiles is given in Figure 36. In making these simulations, all the coefficients determined in the first experiment were used, with the exception of σ_{max} which was re-evaluated for the new target material. No profile simulation is given for the lowest velocity shot because no hole enlargement was predicted. Excellent agreement is obtained at the three highest velocities. The experimental and theoretical values of the maximum penetration are listed in Table IV and also shown graphically in Figure 37. The agreement with experiment is generally good. As the velocity is decreased, the simulation gives depths that are too high, primarily because it does not predict crater enlargement as great as is obtained experimentally. It was found that σ_{max} = 500,000 lb/in^2 gave the best agreement with experiment.

Experiment No. 4

This experiment was similar to No. 3, except that the target was made of substantially harder steel (i.e. BHN 302 compared to 125). The projectiles remained unchanged, but were fired at velocities from 1900 ft/s to 3900 ft/s. Radiographs of the craters are shown in Figure 38, and a comparison between the experimental and predicted profiles is made in Figure 39. It was found that at the highest velocity normal hole enlargement did not occur because of projectile break-up. This resulted in the brittle equivalent of hydrodynamic flow of a ductile projectile (Ref. 9) and the formation of a relatively large and constant diameter crater. As might be expected, there was a noticeable decrease in the penetration depth. Of the remaining four shots, very good profile matching was obtained at the two higher velocities. At the lower velocities, virtually no crater enlargement was predicted. It should be emphasized, that the theoretical model does not attempt to describe the surface 'crown' crater, but only the hole enlargement which takes place below the original surface. In Figure 40 and Table V, a comparison is made between the experimental and predicted depths of penetration. Once again, the agreement is good enough to allow the simulation to be used for comparative design studies. However, as with the previous steel target, the simulated crater growth at low velocity is not as extensive as is found experimentally. Hence, the simulated depths are too large. The value of σ_{max} determined for this target material was 800,000 lb/in^2.

Experiment No. 5

In the last formal experiment, an attempt was made to use the coefficients determined for conical profiles of various β, to predict the penetration and cratering phenomena associated with the impact of a family of doubly-tapered projectiles (Figure 12). In this experiment, the original target material (Aluminum Type 1) was impacted with steel projectiles of $\beta_1 = 60°$ and $\beta_2 = 10°$ having tip diameters varying from 0.20 to 0.40 inch. Tests were made at two velocity levels with each type of projectile. Exceptionally good impacts were obtained in all cases, with virtually no yaw either on impact or during penetration of the target. All profiles are shown both radiographically and graphically in Figures 41 to 52. On comparing the predicted profiles with experiment, we find that in general the agreement is good, particularly for the smaller values of tip diameter. In these cases ($d_t = 0.2$, 0.24 and 0.28) the model accurately predicted that there would be little enlargement of the crater. For the higher values of d_t, the relative volumes of the enlarged craters were more closely simulated than their actual profiles. This of course reflects the fact that even for a singly-tapered projectile of $\beta_1 = 60°$, the model did not accurately simulate the diameter/depth gradient. On the other hand, as indicated by Table VI, the largest error in the computed penetration for all of these projectiles was only 9.4%, with the closest matching occurring for the larger values of d_t. It should also be noted that the diametral scale used for all comparisons has been intentionally exaggerated to point out the detailed differences between predicted and experimental profiles. To indicate the true-scale behaviour of the simulation, the comparison in Figure 50 is also shown with real dimensions.

DISCUSSION

The results obtained in the five experiments described in the previous section allowed the evaluation of the coefficients C_β, K_2 and σ_c/σ_{max} as functions of β, as well as the limiting value of the ballistic number N_B^*. In addition, it was shown that these coefficients could be used to predict the profiles and depths of craters for

a) different velocities,

b) different projectile and target materials,

and c) different shapes of projectile.

During the iterative process of establishing the coefficients, their relative influence on different aspects of the crater profile was determined. It was found that for a given projectile velocity and target, that

a) an increase in C_β increases the hole diameter at the surface, has little effect on the depth at which re-attachment occurred and decreases the total depth of penetration,

b) an increase in σ_c decreases the hole diameter at the surface, the depth at which re-attachment occurs and also the total depth of penetration

c) an increase in K_2 decreases the total depth of penetration and the depth at which re-attachment occurs and strongly influences the crater profile

d) an increase in σ_{max} decreases mainly the depth of penetration and also the hole diameter at the surface, and

e) an increase in the ballistic number decreases the depth at which re-attachment occurs (hole enlargement stops) and has no effect on the depth of penetration. This is shown by the broken line profile in Figure 52.

The particular case for which $N_B^* = 0$, represents a simpler model in which no allowance is made for the fact that radial expansion must stop when the inertial pressure of the material moving radially just equals the flow stress.

Because of the scatter in velocities obtained during Experiment No. 1, it was not possible to make direct comparisons between the craters formed by singly-tapered cones of different apical angles. However, with the coefficients obtained by simulation, we can now use the model to compare crater profiles for various β. This is done in Figure 53 for steel projectiles (V_o = 2500 ft/s), impacting the Type 1 aluminum target for $10° < \beta > 90$. As β increases, the crater volume increases until a semi-apical angle of 50° is reached. Beyond 50°, the differences in profile are so small that all remaining profiles can be shown by a single line. The change in depth of penetration with β (Figure 54) is somewhat stronger than the profile variation between 50 and 90° but still small. Clearly, there will not be much difference between projectiles within this range of β. This is of course in keeping with the hypothesis that projectiles with $\beta > 50°$ acquire a cap of stagnant material that effectively changes the semi-apical angle to about 55° and allows the projectile to follow a minimum energy trajectory through the target. To substantiate this hypothesis, two of the Type 1 aluminum targets (β = 60° and 90°) were sectioned and macro-etched to show the flow conditions immediately ahead of the penetrators. These are compared (Figure 55) with the results obtained by the quasi-static punching of a laminated clay target. The similarity between the flow caused by the two flat ended cylinders is striking when one considers that there was a difference of over six orders of magnitude in the penetration rate. The strong similarity between the flow around the 60° and the 90° penetrators is also apparent.

For the 90° penetrator, the stagnation cone is clearly defined by a narrow zone of adiabatic shear. In forming a stagnation cone, the dynamical system is itself selecting a lower energy deformation mode in order to pursue a minimum energy trajectory. One is then immediately faced with the question 'why does the system not select a smaller apical angle?'. As has been shown in this study, deeper penetrations are obtained with smaller values of β i.e. the rate of change of energy along the trajectory decreases with β. One might postulate that smaller apical angles would increase the area of the adiabatic shear surface and cause a greater loss of energy to shear than is saved by the reduction in inertial resistance. However, this argument is not satisfactory, as it can be shown that because of adiabatic heating the interface shear component of resistance for a preformed cone is very small compared to all other components. On the other hand, from the photograph in Figure 55, it is clear that the stagnation cone is behaving exactly like a preformed cone. The only plausible explanation for the selection of 55° is that it represents the smallest apical angle with sufficient structural strength to penetrate a target (of the same material) without deformation.

It should be noted that the 'total' penetration from original surface to the point of the projectile is appreciably greater for $\beta = 50$ to $\beta = 90$ as all measurements of depth in this study are made to the rear shoulder of the penetrator. The use of the rear shoulder in defining penetration is adopted to allow the comparisons made with this type of analysis to be extended to the complete perforation of a finite target. Some discussion of the finite target problem will be given later. Returning to Figure 54, we can see that for projectiles having identical diameter, mass and velocity the penetration (to the shoulder) for $\beta = 10°$ is approximately 56% greater than for $\beta = 90°$. The reason for this of course is that for $\beta = 10°$, much less energy has been expended in crater enlargement. In practical armour piercing projectiles, this advantage cannot be fully realized because of the structural strength required by the very slender nose to prevent deformation on impacting an oblique target. Evidence of this is available in the present study e.g. Figure 29, in which we see that even at at normal impact, the nose of the penetrator ($\beta = 10°$), has been deformed during penetration and some projectile yaw has occurred inside the target. In addition to projectile deformation, it is well known that blunter nose-profiles are less prone to ricochet on impacting an oblique target. A shape that has frequently been used is the doubly-tapered conical nose. We are now in a position to investigate theoretically the possibility of designing a double-tapered projectile such that the crater enlargement is kept to a minimum while still presenting a relatively blunt nose-profile. It should be emphasized that for any given impact velocity there will be an optimum projectile configuration that depends on the target material. Simulated profiles have been computed for a set of doubly-tapered steel projectiles having $\beta_1 = 60°$ and $\beta_2 = 10°$. The mass and diameter were the same as those used experimentally and the tip diameter ratio was varied from 0.2 to 0.4. These profiles, which

are compared in Figure 56, show that minimum crater volume will occur with a tip diameter ratio of approximately 0.65. If we now look at the penetrations (Figure 57) associated with these profiles, we find, that the smallest crater volume is not always indicative of the maximum penetration. However it can also be seen for this particular velocity, that a value of d_t/d_c close to 0.6 would give approximately 70% of the penetration advantage of the pure 10° projectile and at the same time provide a relatively blunt nose profile. If the velocity level is raised, it is probably better to have a smaller tip diameter. If it is lowered, then the tip diameter can be increased.

Experimentally, we found that the predicted crater profiles for doubly-tapered projectiles were not as good as the single-taper simulations. In most cases, the diameter at the surface was larger than expected. this may be explained in the following way. In the analytical model, it is assumed that if the instantaneous velocity is high enough, the material that is accelerated laterally from the front shoulder will reach a diameter larger than the body diameter and hence will never come into contact with the near shoulder. Perhaps this idealization is not justified. As soon as the material leaves the front shoulder, it begins to decelerate. Thus as the instantaneous hole diameter approaches the final value, the radial velocity of the material also approaches zero. It is therefore to be expected that combinations of geometry and velocity exist for which re-attachment on the rear shoulder will occur, not because of inadequate lateral acceleration, but because of insufficient time for the target material to get out of the way of the incoming rear shoulder. Such a secondary impact would of course impart an additional radial acceleration and produce a larger diameter hole than would be predicted by the model. It would be entirely possible to include this time-dependent behaviour in the model. It is felt however, the increase in complexity would far outweigh any increase in accuracy or predictive capability.

The following comments relate to the general theme of the study though not specifically to the five main experiments. It is always of interest in any analytical study of the penetration process, to look at the variation of depth with impact velocity for a given projectile-target combination. One of the most common 'rule-of-thumb' criteria, is that the depth penetrated is directly proportional to the ratio of total kinetic energy to cross-section area. This is of course derived directly from the assumption that the target flow stress is constant and that there is no hole enlargement. An equivalent criterion is the proportionality between kinetic energy and total hole volume which allows for the possibility of the hole enlargement, but requires a knowledge of the profile before it can be applied. If we look at Figure 58, we see that when both the variation in flow stress and hole enlargement are considered, the functional relationship between total depth and impact velocity depends on the angle β. The indicated threshold velocity at zero depth of penetration again reminds us that the depth is being measured from the shoulder and that zero depth corresponds to total

immersion of the nose. We may conclude for the case of $\beta>50°$, that projectile momentum is of much greater importance than kinetic energy. As β decreases, hole enlargement becomes less dominant in the penetration process and the depth shows a higher order dependence on velocity, particularly at the lower velocities. As velocity increases, an increasing proportion of the energy is used in hole enlargement (Figure 59), and the rate of increase of depth with velocity decreases. These results show clearly that there is no simple criterion which can be used to relate penetration and impact velocity for all β unless the profile is known, in which case, an assumption of proportionality between energy and volume will give a good first approximation. The relationship between depth and velocity may be approximated by an equation of the form

$$P_m = KMV^{n(\beta V)},$$

where the exponent n is itself a function of both β and V. For small β and V, n will approach a value of 2, yielding the kinetic energy criterion. However, if either β or V is large, the exponent tends toward unity. As we have seen previously, for $\beta>50°$, there is little difference between the hole profiles. Hence we might expect the value of N to be approximately the same for all values of β above 50°.

The phenomenon of secondary crater growth for doubly-tapered penetrators was postulated during the development of the simulation. Although this behaviour was not encountered experimentally, the computer code is at least able to simulate it. Figure 60 shows the predicted crater profile for a doubly-tapered steel projectile ($\beta_1 = 40°$, $\beta_2 = 30°$, $d_t = 0.27$) impacting a Type 1 aluminum target at 2500 ft/s. The secondary separation, caused by re-attachment of the primary separated flow on the rear shoulder, is quite evident. The case shown is quite extreme, i.e. $\beta_1 \tilde{\approx} \beta_2$ and indicates that in practice, secondary separation will not be a major cause of crater growth, particularly for cases in which $\beta_1 >> \beta_2$.

As a further test of the predictive capability of the simulation, one of the singly-tapered tungsten carbide projectiles used in experiments No. 2 and 3 was tested against an aluminum Type 1 target. A radiograph of the penetration is shown in Figure 61 and a comparison is made in Figure 62 between the experimental profile and the computer simulation. The coefficients used for this simulation were those developed with steel projectiles in the first experiment (Table VI). The agreement with experiment is exceptionally good, particularly with respect to the depth, which was predicted to within 2.6%. Although it is evident from Figure 61 that the projectile tip passed through the rear surface of the target, it is doubtful if this significantly affected the penetration since the target was mounted on a backup plate of the same material. This shot is of particular interest in that it lends support to the physical significance of N_B^* and the

value determined previously. If we compare this profile to the one obtained with a lighter steel projectile at a similar velocity (Figures 19 and 20), we see that the re-attachment is well simulated in both cases even though there is almost a two inch difference in the total depth. It is clear that N_B^* must be dependent only on the penetration mode.

Finally, some consideration should be given to the application of this simulation to the perforation of finite targets. Clearly, if we consider relatively thin targets, (of the order of on projectile diameter in thickness), the model would be of little use in that most of the deformation would be related to the entry and exit phases of the perforation. As it has already been shown that the simulation of the entry phase is perhaps the weakest part of the model, it is very unlikely that exit simulations would be any better. On the other hand, if the target is finite but of several diameters thickness, a successful simulation of the perforation process should be possible by redefining the stress function to allow for stress relaxation caused by proximity of the rear surface. Previously we defined the variation in flow stress as

$$\sigma(x) = \sigma_{max}\left(1-\left(1-\frac{\sigma_c}{\sigma_{max}}\right)e^{-KX/d_c}\right) ,$$

which says that the stress at the front surface (x = 0) is σ_c and that it approaches σ_{max} asymptotically at great depth. If we now consider a finite target of thickness t_T, a first approximation to the appropriate stress function can be written down by assuming that the stress will vary in the manner described by equation 18 from both sides of the target i.e.

$$\sigma(x) = \sigma_{max}\left(1-(1-\sigma_c/\sigma_{max})e^{-KX/d_c}\right),\ x< t_T/2 \qquad (24)$$

$$\sigma(x) = \sigma_{max}\left(1-(1-\sigma_c/\sigma_{max})e^{-K(t-x)/d_c},\ x> t_T/2\right)$$

Equations 24 will yield a maximum resistance at the center of the target and values of $\sigma(x) = \sigma_c$ at the front and back surfaces. As previously mentioned, a value of $X = t_T$ would represent the complete passage of the shoulder of a conical projectile through the target.

CONCLUSIONS

1. The penetration and cratering process for non-deforming projectiles impacting ductile targets has been analytically modeled on the basis of an aerodynamic analogy involving a rigid-plastic 'atmosphere'.

2. A set of coefficient (C_β, σ_c/σ_{max} and K_2), describing the resistance of this 'atmosphere' to conical projectiles, have been defined as functions of the semi-apical angle for $0<\beta<90°$.

3. A non-dimensional ballistic number N_B, (instantaneous dynamic inertial pressure/local flow stress) has been defined. It is shown that below a critical value ($N_B^* = 0.5$), target separation will not occur, i.e. the crater diameter will equal that of the projectile.

4. It is shown by comparison with experiment that the model can give good simulations of the crater profiles for the following projectile/target combinations: Steel/ soft aluminum, tungsten carbide/ soft aluminum, tungsten carbide/ mild steel and tungsten carbide/ AISI 4340 steel (BHN 302).

5. For a given velocity and mass of projectile, the depth of penetration varies strongly with β. For example, the depth is 50% greater for $\beta = 10°$ than for $\beta = 55°$.

6. It is shown that for $\beta > 55°$, there is virtually no difference in the hole profiles produced at a given velocity. In addition, the rate of change of penetration with β is small.

7. For $\beta > 55°$, a conical stagnation zone is formed ahead of the penetrator which effectively changes the semi-apical angle to 55°. This stagnation cone allows the projectile to follow a minimum energy trajectory through the target.

8. The model can be used to predict the target response to a doubly-tapered penetrator and allows the design of a relatively blunt projectile to minimize ricochet while giving the deep penetration of a slender cone. Conversely, if an excess of kinetic energy is available, a projectile can be designed to produce the largest hole possible while still maintaining adequate penetration

9. Finally, for a specified thickness of a given target material, the model allows a rapid comparison to be made between a wide variety of projectiles of singly or doubly-tapered profiles.

ACKNOWLEDGEMENTS

The author wishes to acknowledge the assistance of Mr. Y. Martel and Mr. Y. Pare in the supervision of the target preparation, ballistic testing, radiography and measurement of crater profiles. The painstaking work of Mr. R. Fiset and Mr. R. Lasonde in preparing the laminated clay targets for quasi-static punching experiments is also acknowledged.

REFERENCES

1. Paul, B. and Zaid, M., "Normal perforation of a thin plate by a truncated conical projectile". J. Franklin Inst. 265 (4) 1958.

2. Recht, R.F. and Ipson, T.W., "Ballistic perforation dynamics". J. App. Mech. 30 (3) 1963.

3. Brooks, P.N., "On the penetration of truncated cones into ductile targets". DREV R-665/72, June 1972, Unclassified.

4. Zaid, M. and Paul, B., "Mechanics of high speed projectile perforation". J. Franklin Inst. 246 (8) 1957.

5. Brooks, P.N., "On the penetration of hypervelocity projectiles". DREV TR-492/64, April 1964, Unclassified.

6. Allen, W. and Rogers, J., "Penetration of a rod into a semi-infinite target". Journal of the Franklin Institute, Vol 272, No 4, Oct 1961.

7. Slaght, W., Private communication, DREV, 1972.

8. Mulhearn, T.O., "The deformation of metals by Vickers-type pyramidal indenters". Journal of the Mechanics and Physics of Solids, Vol 7, 1959.

9. Brooks, P.N. and Erickson, W.H., "The ballistic evaluation of materials for armour penetrator". DREV R-643/71, November 1971, Unclassified.

TABLE I - Target Characteristics

Type	Material	.2% Y.S. (lb/in^2)	U.T.S. (lb/in^2)	Elong. (%)	Red Area (%)	Hardness BHN
1	Alum 65-S	6700	17650	35	51	38
2	Steel 1020	46500	61000	28	49	125
3	Steel 4340	132000	150000	17.5	57	302

TABLE II - Experiment No 1

Projectile - Singly-tapered conical

Steel, non-deforning, 398 grains

Target - Aluminum Type 1

β (°)	Velocity (ft/s)	P_m(exp.)* (in)	P_m(theo.) (in)
10 †	2500	>5.40	5.43
15	2436	5.00	4.84
20	2494	4.67	4.68
25	2521	4.39	4.46
30	2601	4.48	4.44
40	2528	3.92	4.00
50	2466	3.58	3.65
60	2541	3.63	3.63
90	2488	3.40	3.44

* Penetration depth was measured from the original surface to the shoulder of the projectile.

† Data questionable because of deformation of the point of the projectile (see Figure 29).

TABLE III - Experiment No 2.

Projectile - Singly-tapered conical

Steel, non-deforming, 398 grains

Target - Aluminum Type 1.

β (°)	Velocity (ft/s)	P_m(exp.)* (in)	P_m(theo.) (in)
10 †	2132	4.14	4.207
15	2114	3.73	3.91
20	2169	3.65	3.84
25	2146	3.36	3.61
30	2198	3.33	3.60
40	2157	3.00	3.28
50	2119	2.81	3.0
60	2075	2.64	2.83
90	2041	2.54	2.71

† Projectile point deformed during penetration

TABLE IV - Experiment No 3.

Projectile - Singly-tapered conical, $\beta = 30°$

Tungsten carbide, non-deforming, 582 grains

Target - Steel Type 2, σ_{max} = 500,000 lb/in^2

Velocity (ft/s)	P_m(exp) (in)	P_m(theo) (in)
1653	.72	.85
1930	.96	1.07
2418	1.44	1.45
2674	1.74	1.65
2985	2.08	1.89

TABLE V - Experiment No 4.

Projectile - Singly-tapered conical, $\beta = 30°$

- Tungsten carbide, non-deforming, 582 grains

Target - Steel Type 3, $\sigma_{max} = 800{,}000$ lb/in^2

Velocity (ft/s)	P_m(exp) (in)	P_m(theo) (in)
1908	.62	.72
2345	.93	1.003
2990	1.42	1.390
3418	1.82	1.647
3899	1.72 †	1.990

† Projectile shattered during penetration

TABLE VI - Experiment No 5.

Projectile - Doubly-tapered conical

$\beta_1 = 60°$, $\beta_2 = 10°$

Steel, non-deforming, 398 grains

Target - Aluminum Type 1

d_t/d_c	Velocity (ft/s)	P_m(exp) (in)	P_m(theo) (in)
.5	2481	4.85	5.04
.6	2475	4.55	4.84
.7	2575	4.58	4.86
.8	2829	5.06	5.035
.9	2574	3.98	3.91
1.0	2512	3.61	3.60
.5	2004	3.25	3.48
.6	2016	3.10	3.39
.7	2200	3.48	3.73
.8	2070	2.92	3.07
.9	2018	2.67	2.74
1.0	2010	2.52	2.73

TABLE VII - Experimentally determined coefficients

N_B^* = 0.50

σ_{max} = 87500 lb/in^2 (Aluminum target, Type 1)

$\beta(^\circ)$	C_β	K_2	σ_c/σ_{max}
10 †	0.29	1.10	0.183
15	0.46	0.90	0.274
20	0.63	0.75	0.360
25	0.80	0.62	0.457
30	0.93	0.505	0.549
40	1.15	0.35	0.731
50	1.32	0.24	0.869
60	1.415	0.161	0.966
90	1.50	0.050	1.000

† Based on extrapolation

Ogival projectile
(a)

Doubly tapered projectile
(b)

FIGURE 1 - Typical projectiles

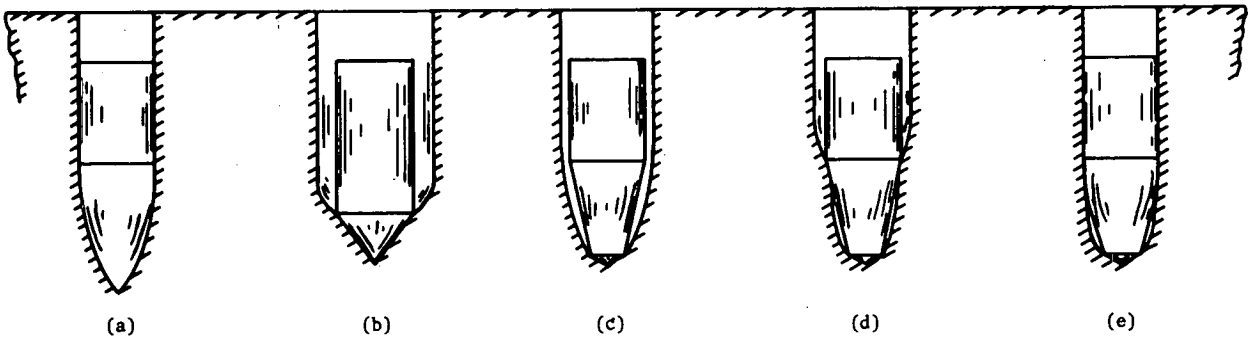

FIGURE 2 - Five possible crater formation modes

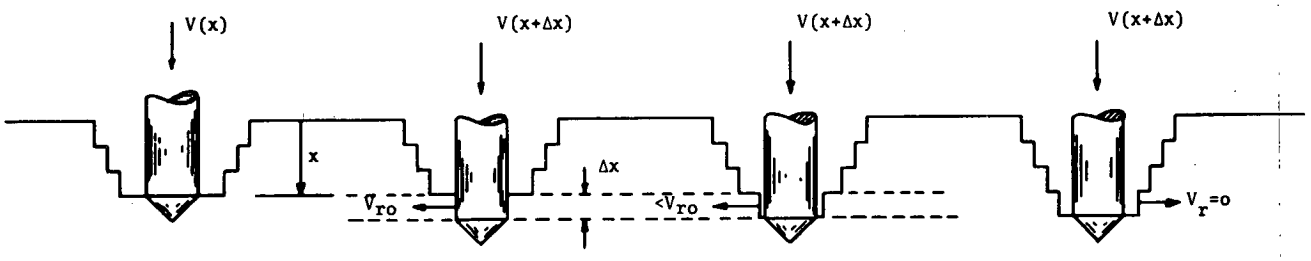

FIGURE 3 - Incremental crater enlargement

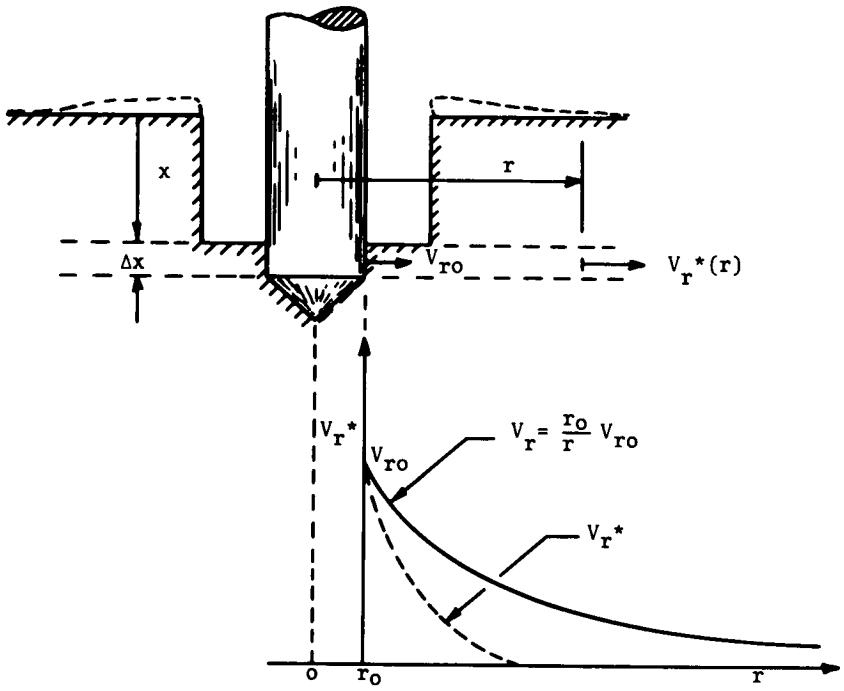

FIGURE 4 - Radial velocity distributions

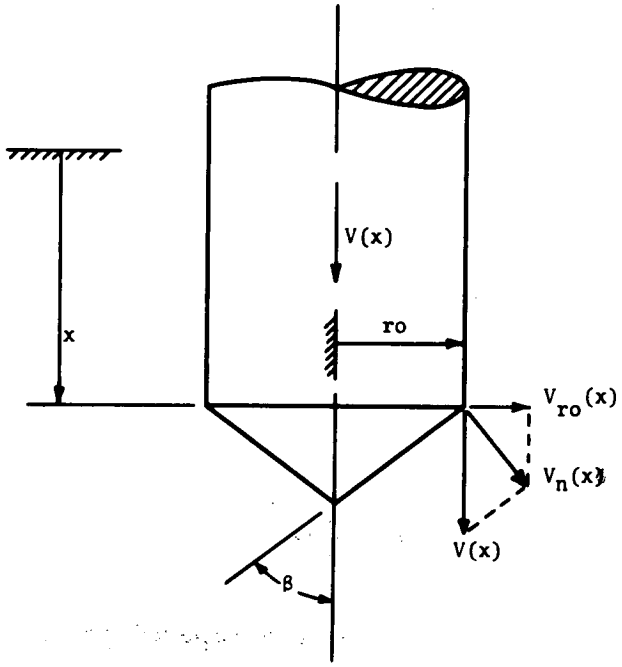

FIGURE 5 - Definition of radial velocity $V_{ro}(x)$

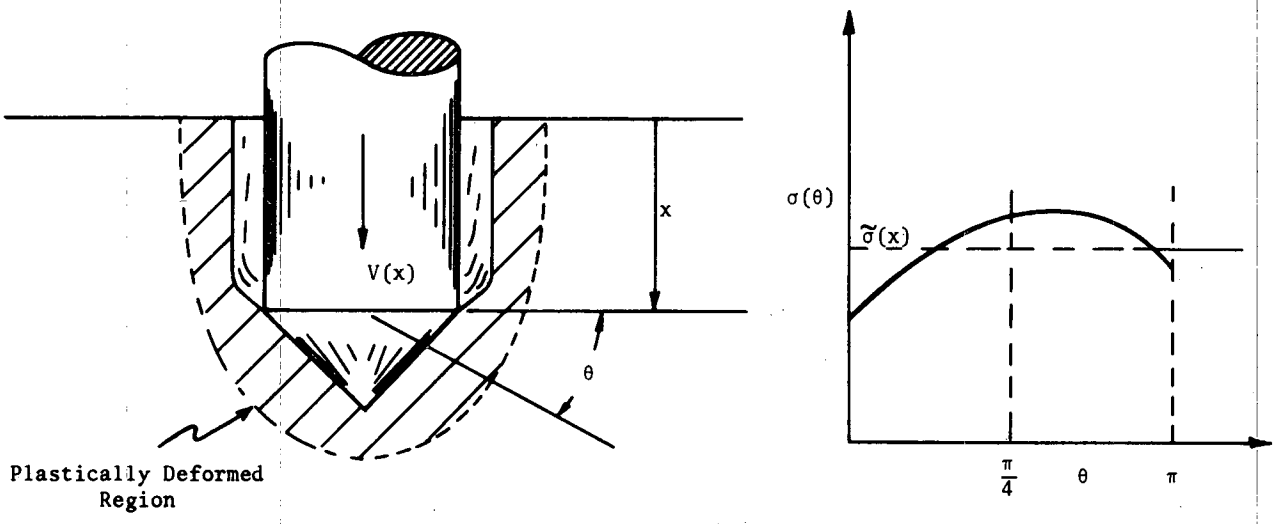

FIGURE 6 - Possible stress and strain distributions

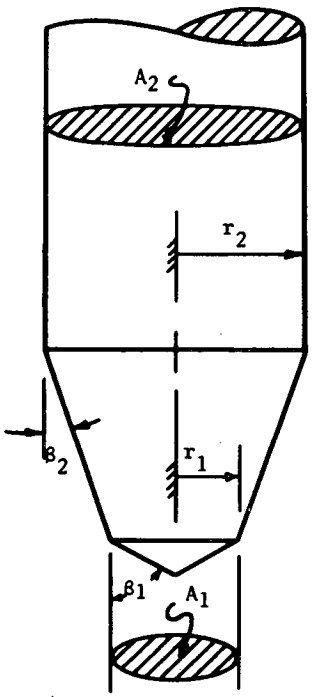

FIGURE 7 - Geometry of doubly tapered penetrator

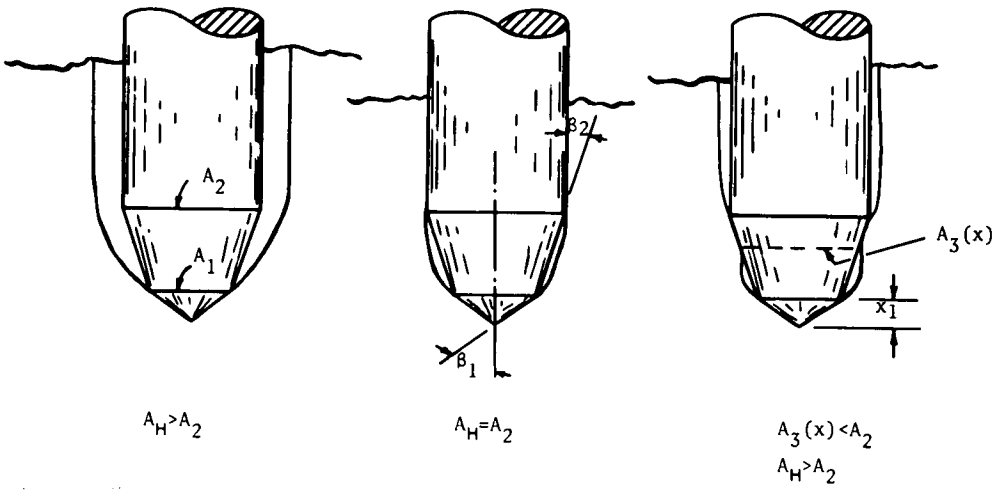

FIGURE 8 - Re-attachment geometry for doubly tapered penetrator

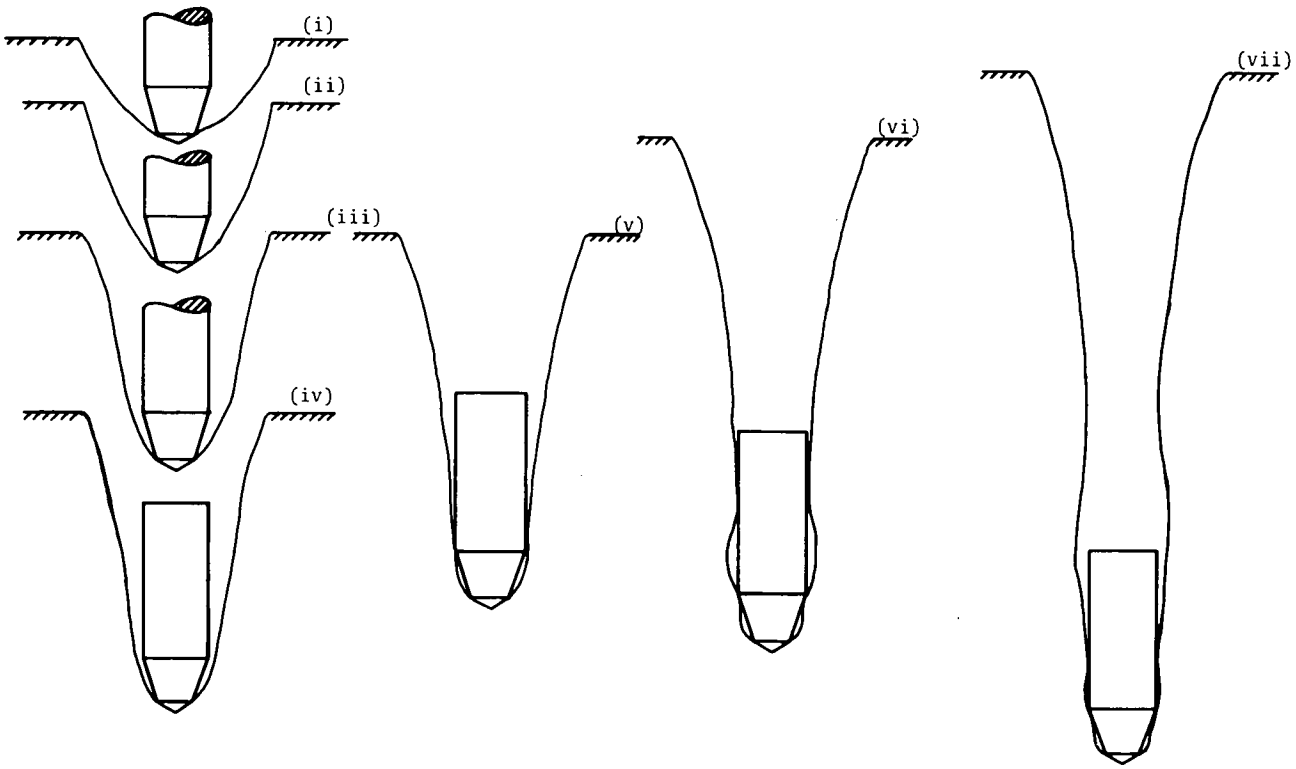

FIGURE 9 - Penetration sequence for doubly tapered penetrator

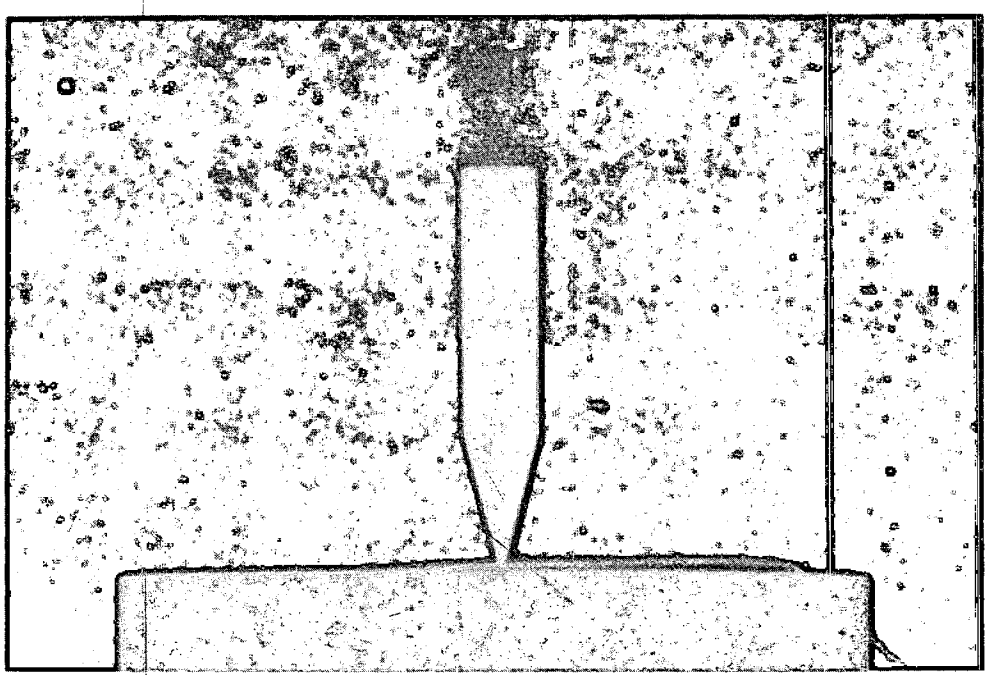

FIGURE 10 - Flash radiograph showing projectile prior to impact

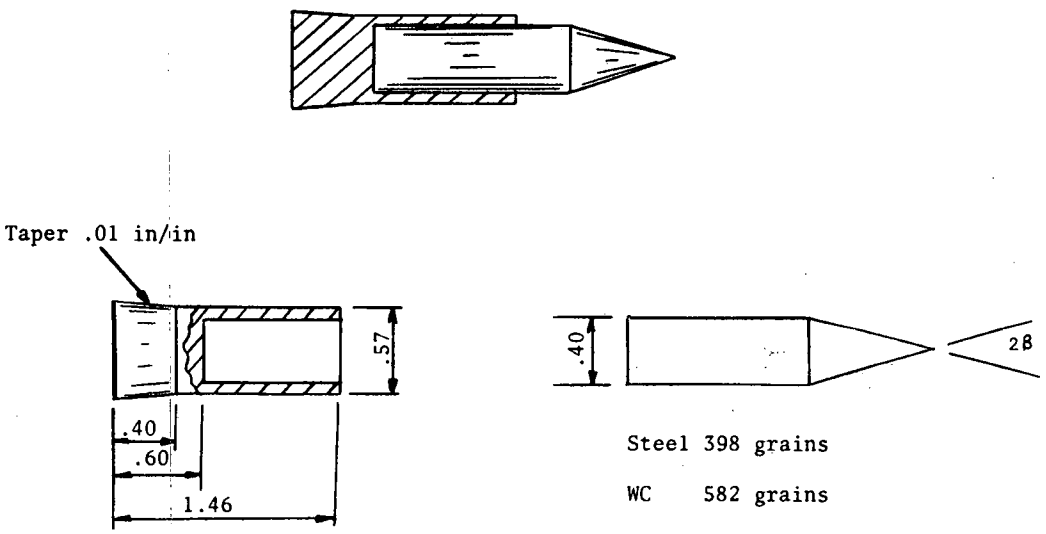

FIGURE 11 - Construction of experimental projectiles

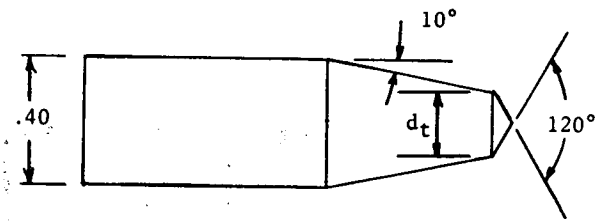

Weight: 398 grains

Type	d_t(in)
1	.2
2	.24
3	.28
4	.32
5	.36
6	.40

FIGURE 12 - Doubly tapered penetrators. Various tip diameters

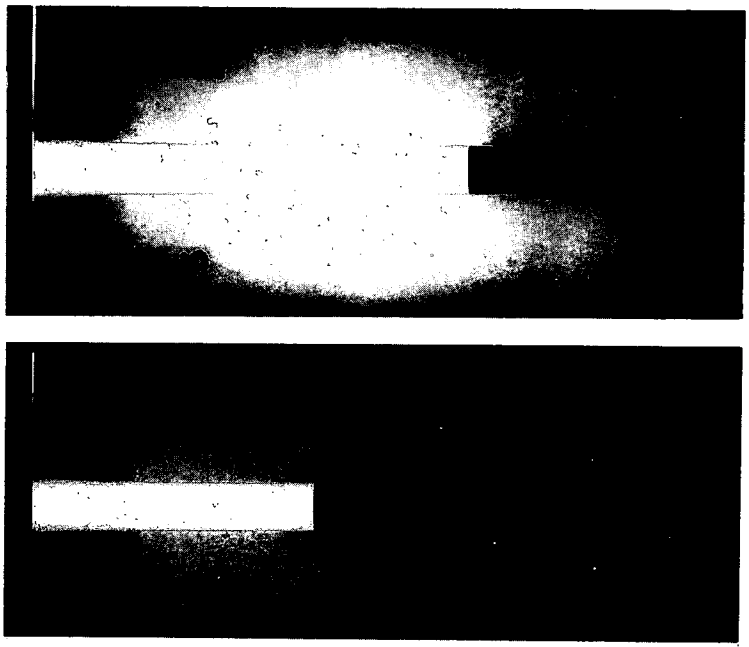

FIGURE 13 - Craters produced by 398 grain singly tapered steel projectile; $\beta = 15°$, V_o = 2436 and 2114 ft/s.
Target, aluminum type 1

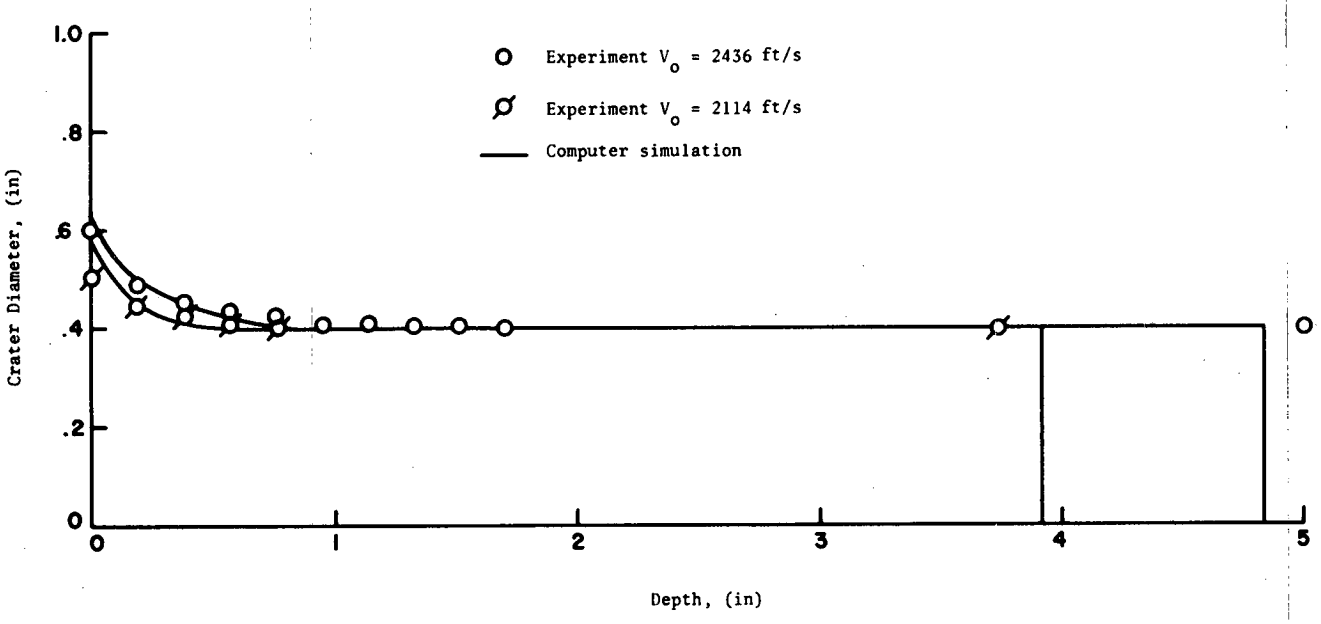

FIGURE 14 - Computer simulations for 398 grain singly tapered steel projectile; $\beta = 15°$, V_o = 2436 and 2114 ft/s.
Target aluminum type 1

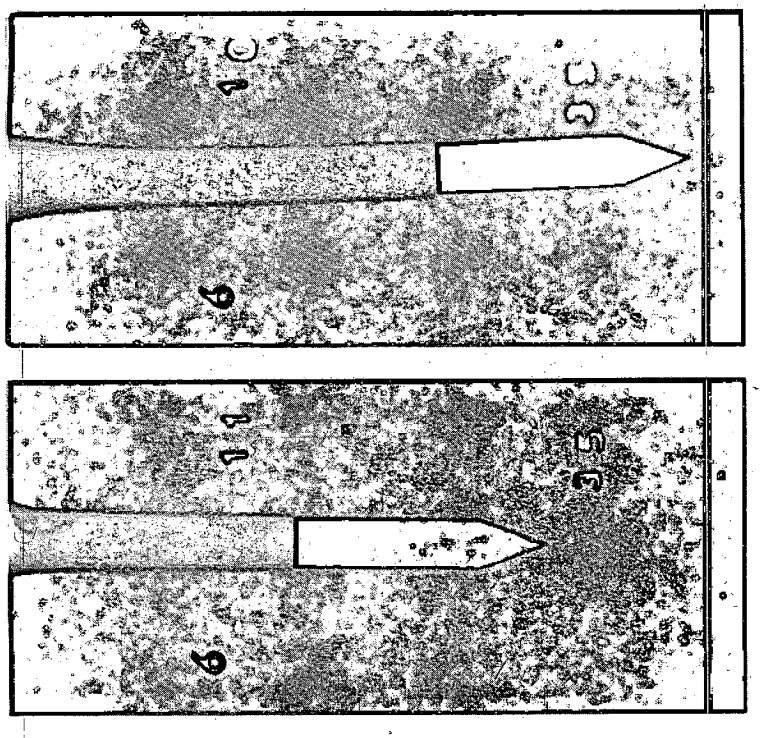

FIGURE 15 - Craters produced by 398 grain singly tapered steel projectile; $\beta = 20°$, V_o = 2494 and 2169 ft/s.
Target, aluminum type 1

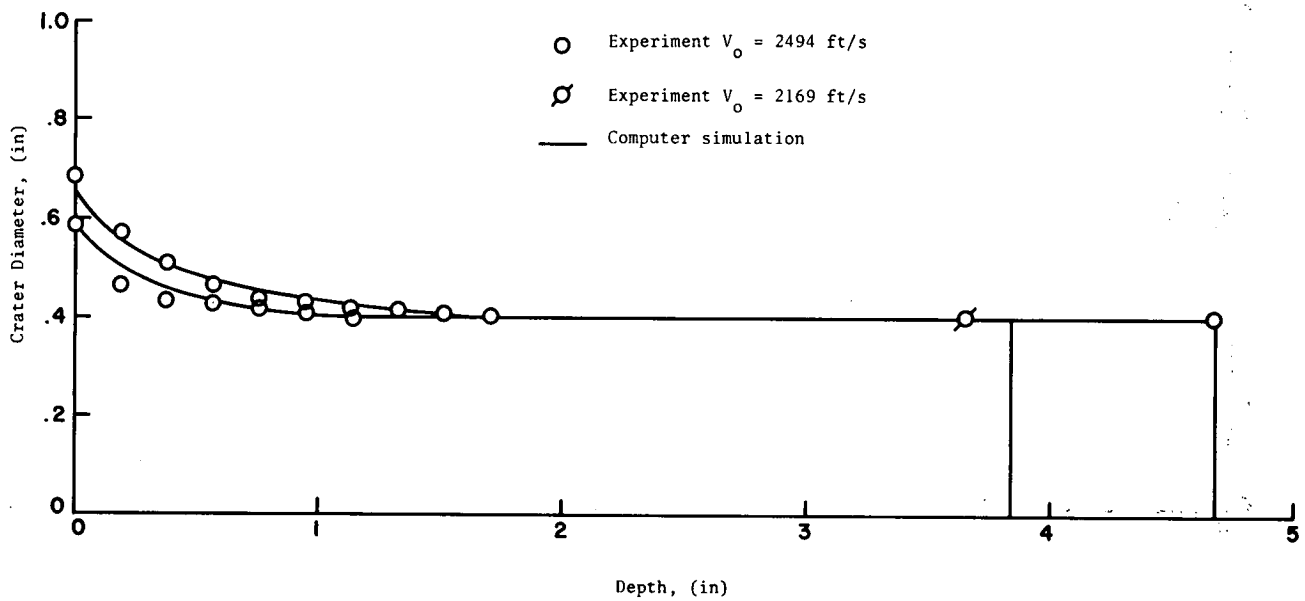

FIGURE 16 - Computer simulations for 398 grain singly tapered steel projectile; $\beta = 20°$, V_o = 2494 and 2169 ft/s.
Target aluminum type 1

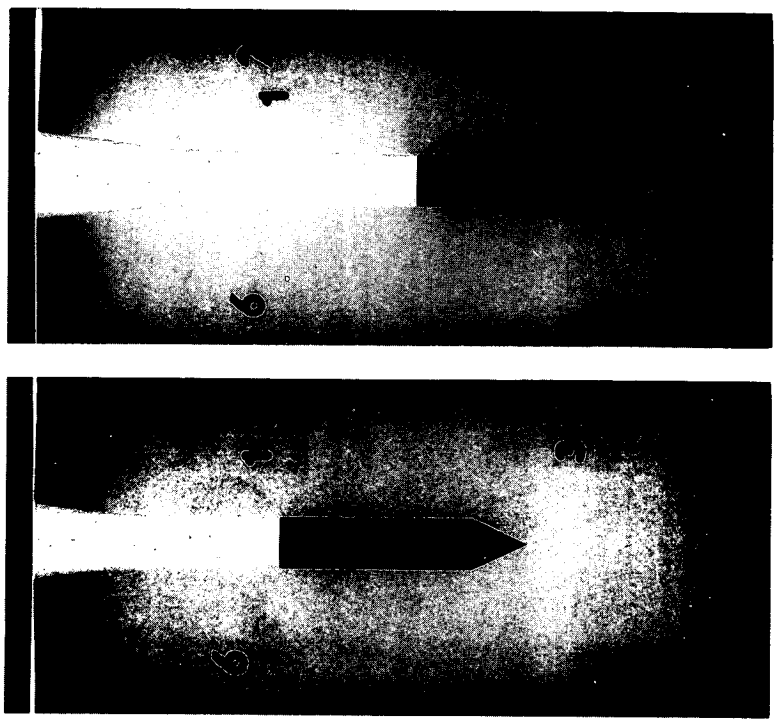

FIGURE 17 - Craters produced by 398 grain singly tapered steel projectile; $\beta = 25°$, V_o = 2521 and 2146 ft/s.
Target,aluminum type 1

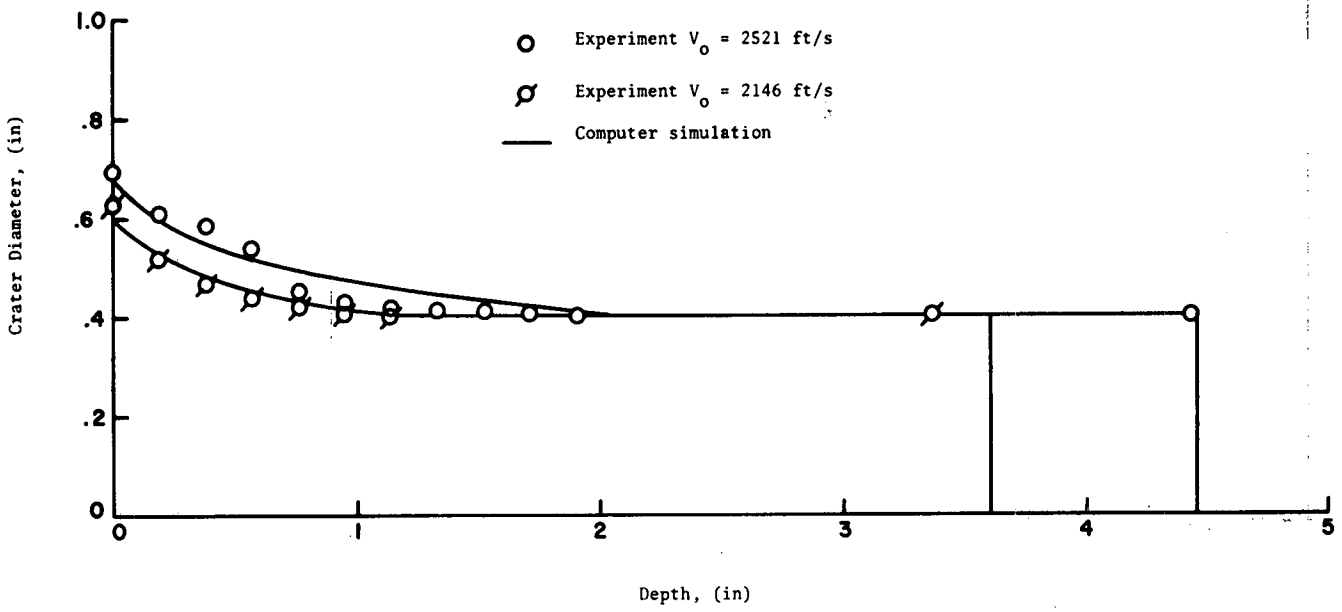

FIGURE 18 - Computer simulations for 398 grain singly tapered steel projectile; $\beta = 25°$, V_o = 2521 and 2198 ft/s.
Target aluminum type 1

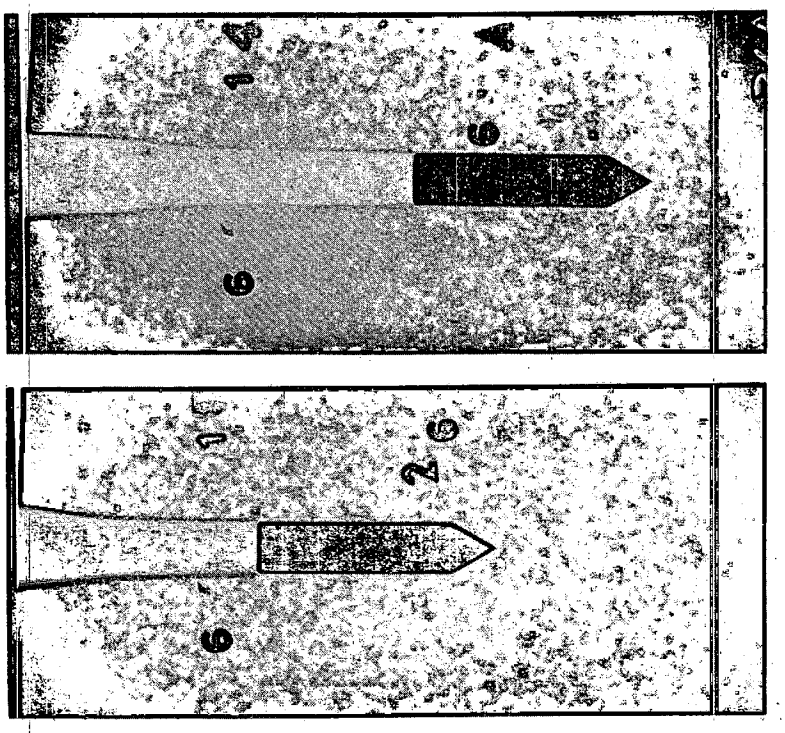

FIGURE 19 - Craters produced by 398 grain singly tapered steel projectile; $\beta = 30°$, V_o = 2601 and 2198 ft/s.
Target, aluminum type 1

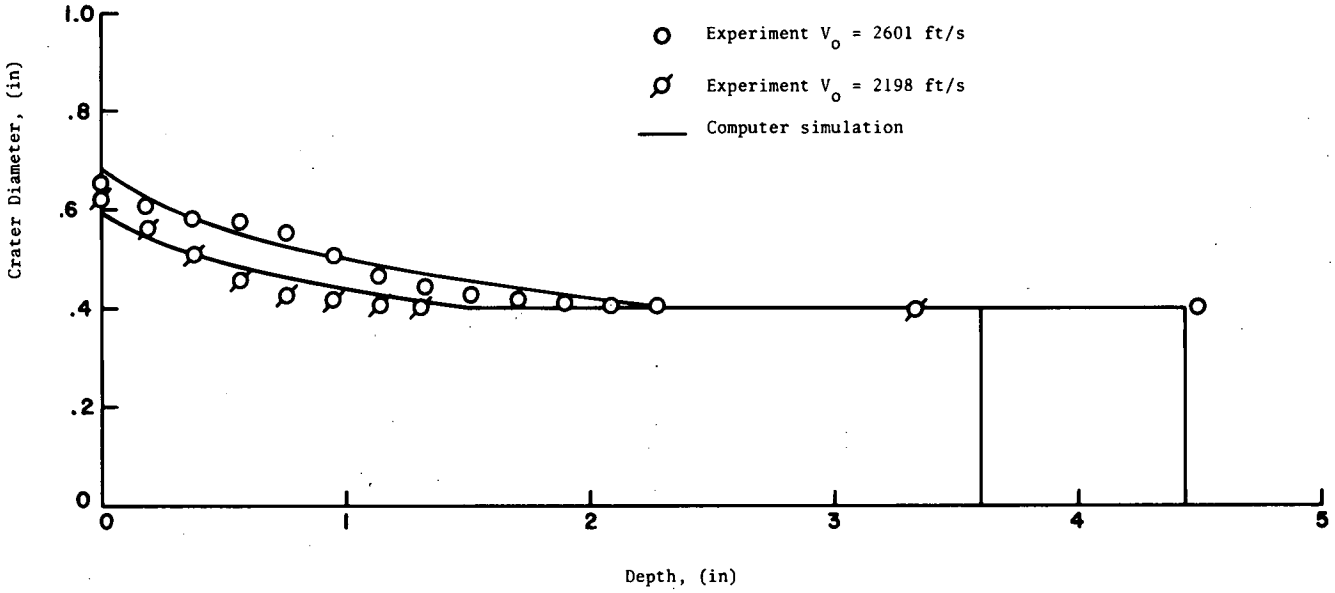

FIGURE 20 - Computer simulations for 398 grain singly tapered steel projectile; $\beta = 30°$, V_o = 2601 and 2198 ft/s.
Target aluminum type 1

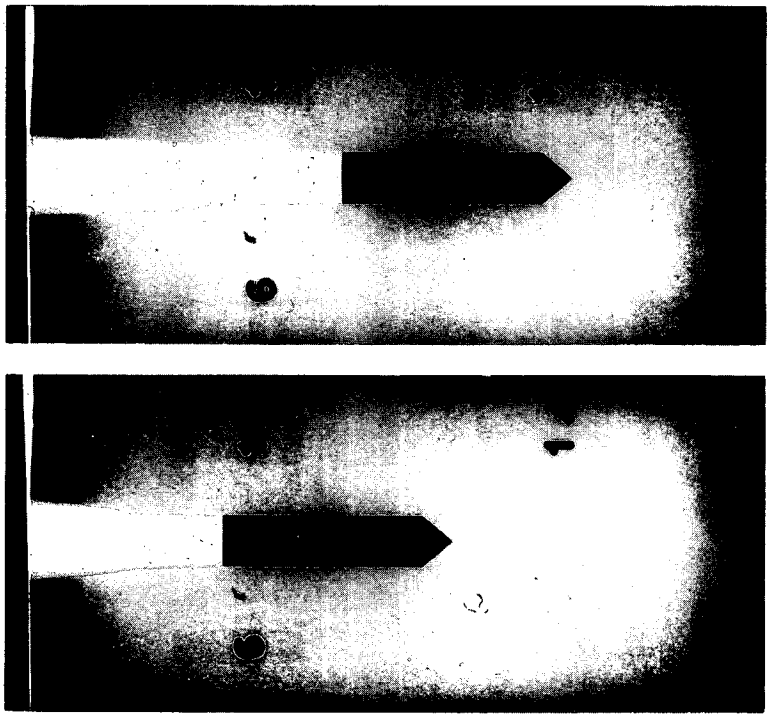

FIGURE 21 - Craters produced by 398 grain singly tapered steel projectile; $\beta = 40°$, V_o = 2528 and 2157 ft/s.
Target, aluminum type 1

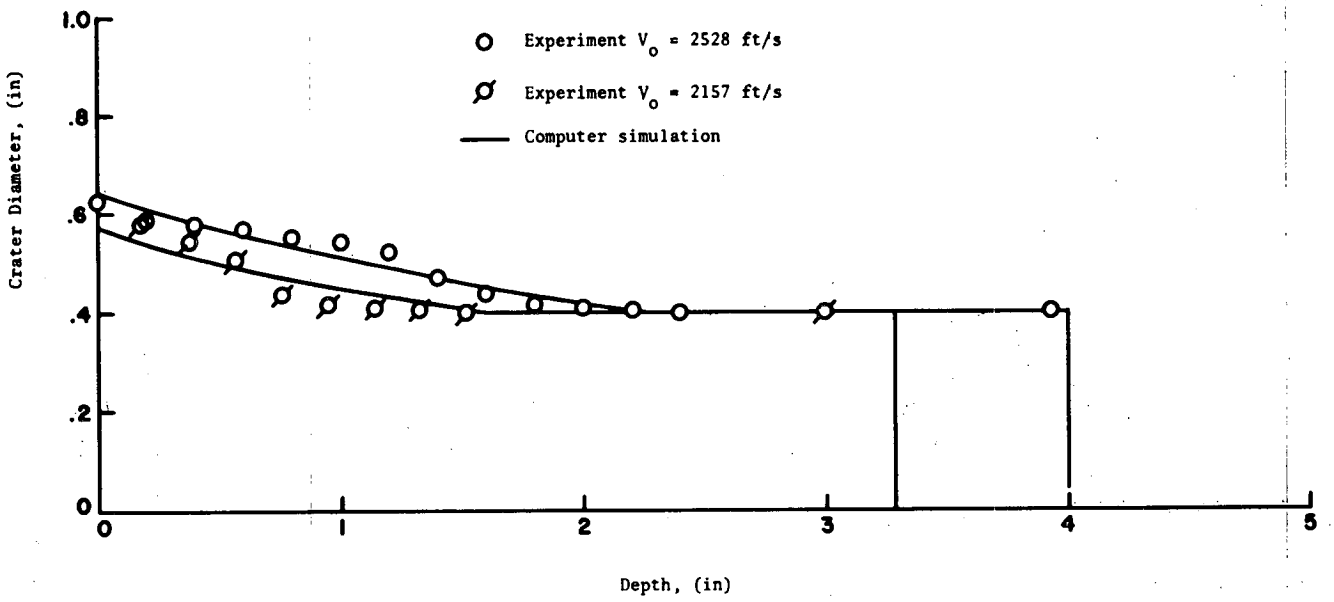

FIGURE 22 - Computer simulations for 398 grain singly tapered steel projectile; $\beta = 40°$, V_o = 2528 and 2157 ft/s.
Target aluminum type 1

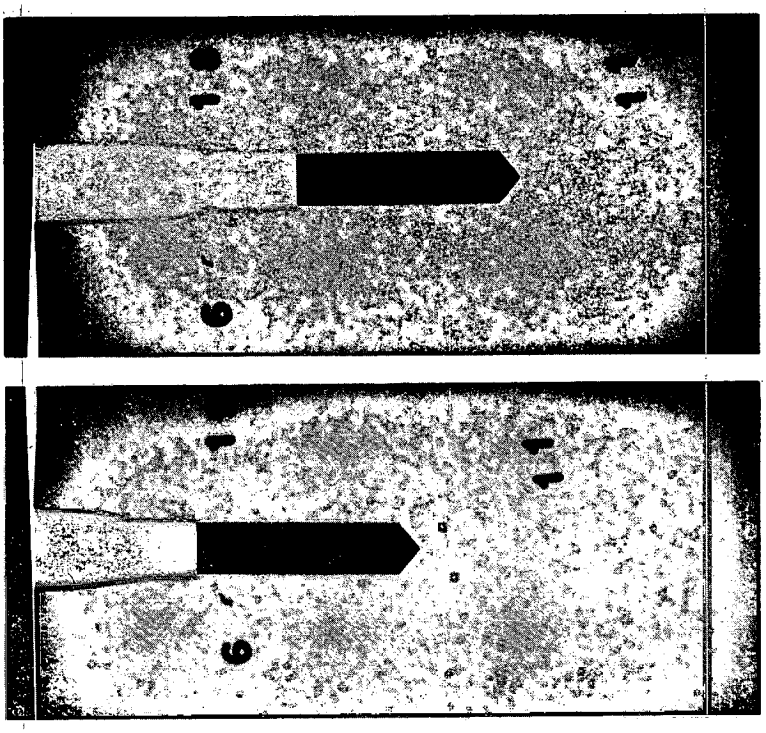

FIGURE 23 - Craters produced by 398 grain singly tapered steel projectile; $\beta = 50°$, V_o = 2466 and 2119 ft/s.
Target, aluminum type 1

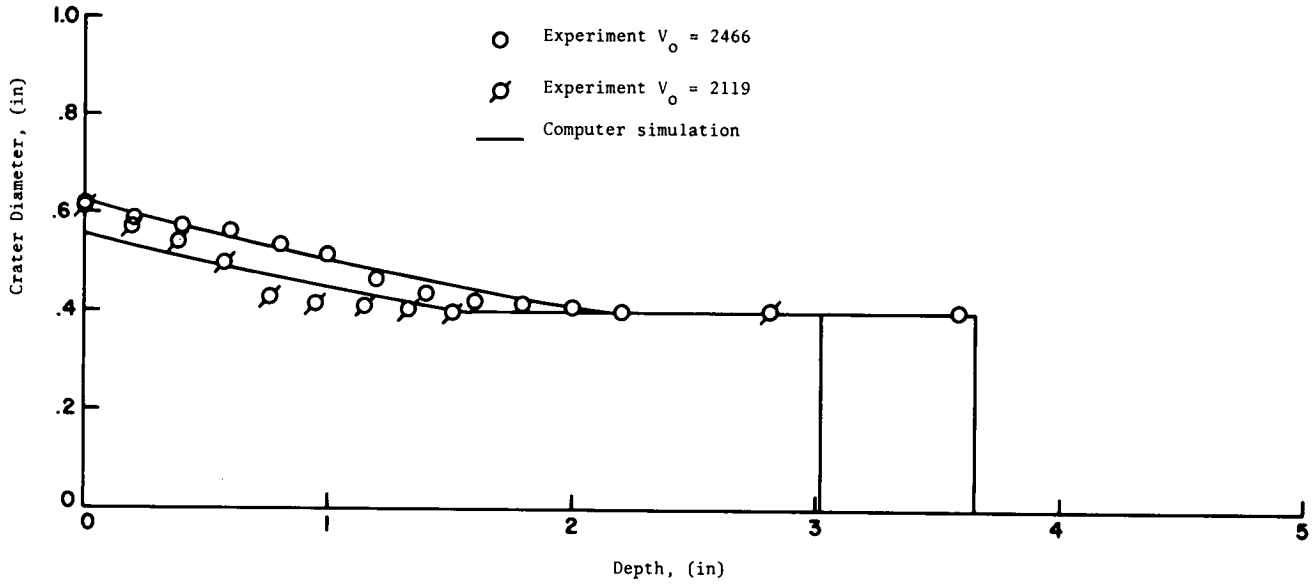

FIGURE 24 - Computer simulations for 398 grain singly tapered steel projectile; $\beta = 50°$, V_o = 2466 and 2119 ft/s.
Target aluminum type 1

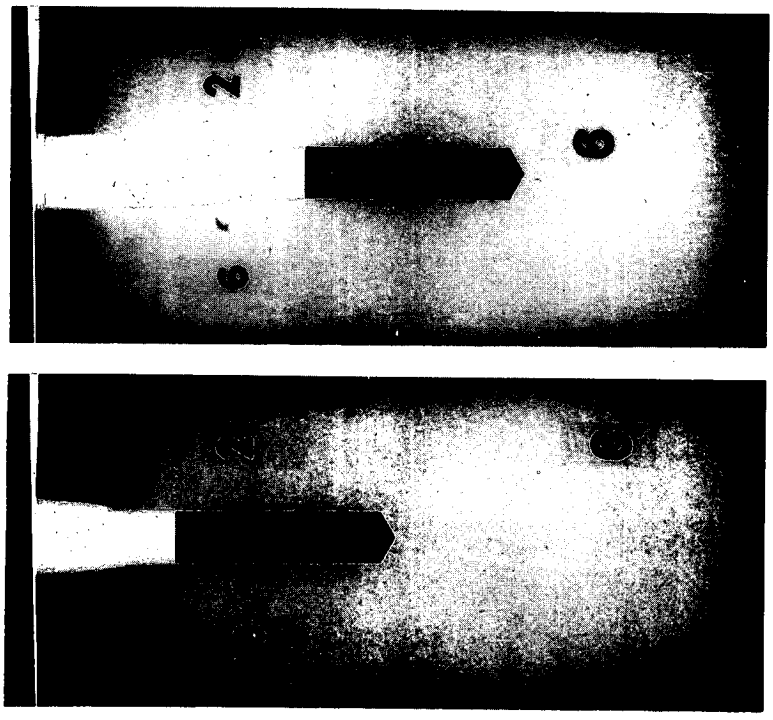

FIGURE 25 - Craters produced by 398 grain singly tapered steel projectile; $\beta = 60°$, V_o = 2541 and 2075 ft/s.
Target, aluminum type 1

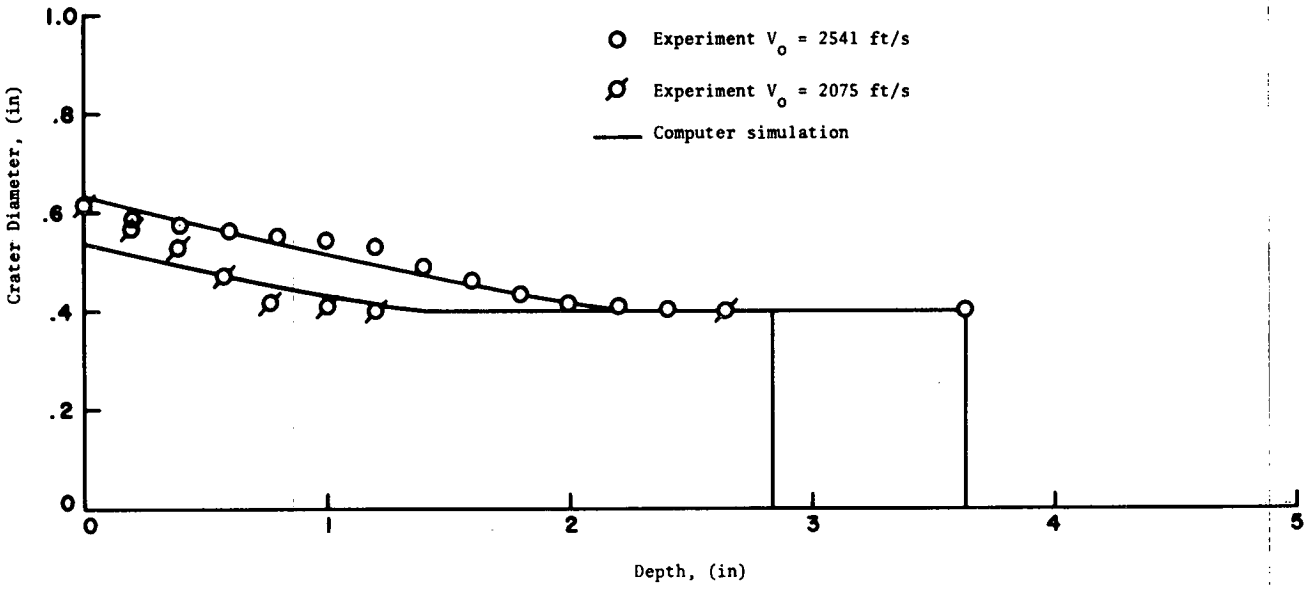

FIGURE 26 - Computer simulations for 398 grain singly tapered steel projectile; $\beta = 60°$, V_o = 2541 and 2075 ft/s.
Target aluminum type 1

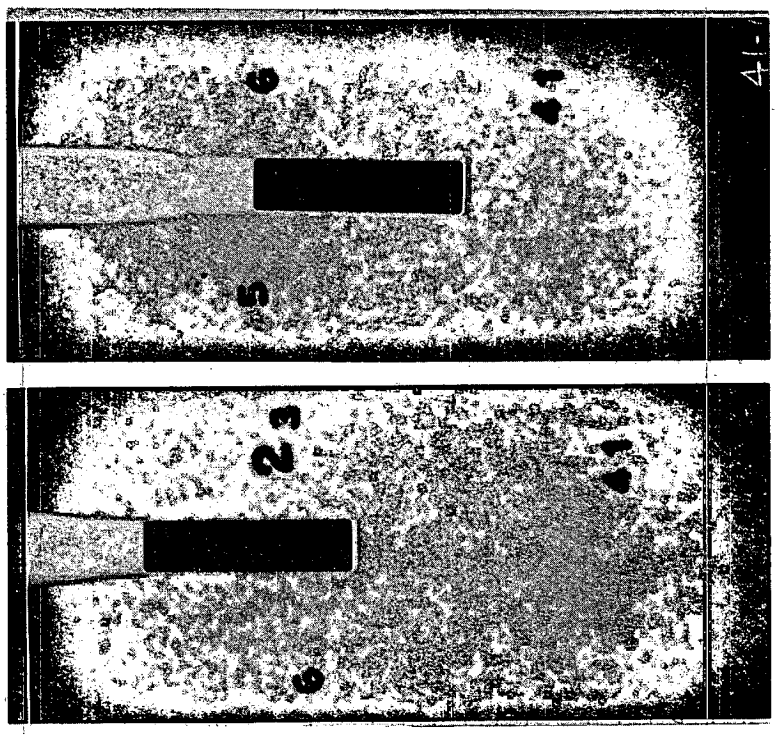

FIGURE 27 - Craters produced by 398 grain singly tapered steel projectile; $\beta = 90°$, V_o = 2488 and 2041 ft/s.
Target, aluminum type 1

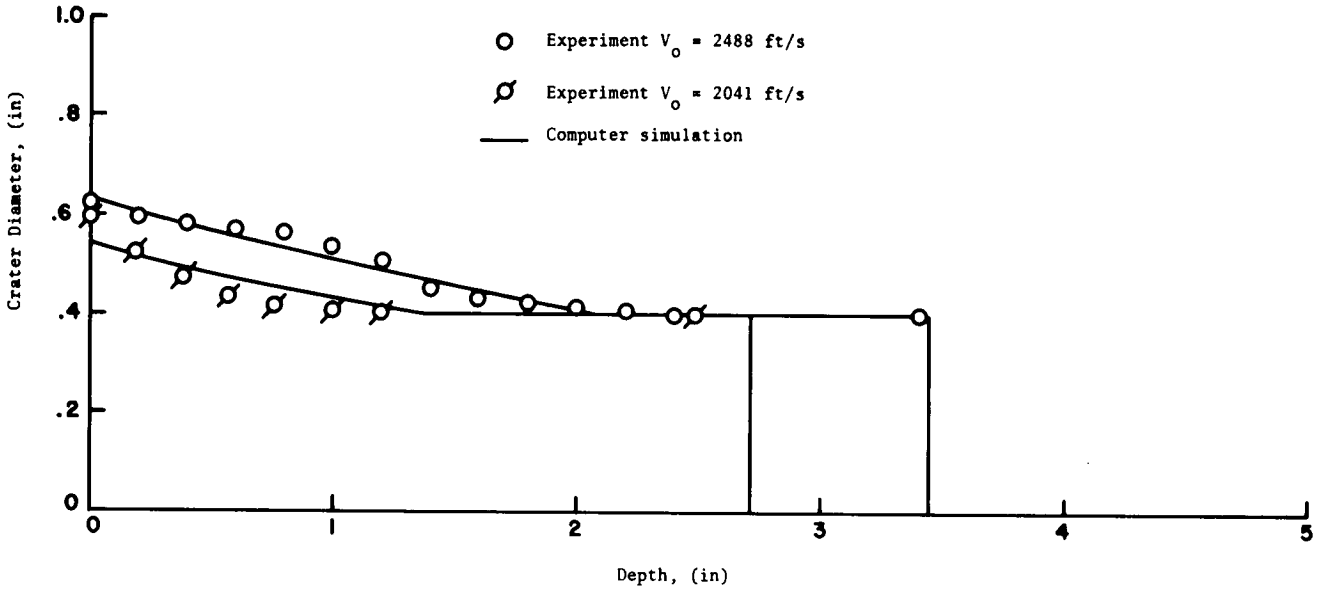

FIGURE 28 - Computer simulations for 398 grain singly tapered steel projectile; $\beta = 90°$, V_o = 2488 and 2041 ft/s.
Target aluminum type 1

FIGURE 29 - Crater produced by 398 grain singly tapered steel projectile; $\beta = 10°$, V_o = 2500 ft/s.
Target, aluminum type 1

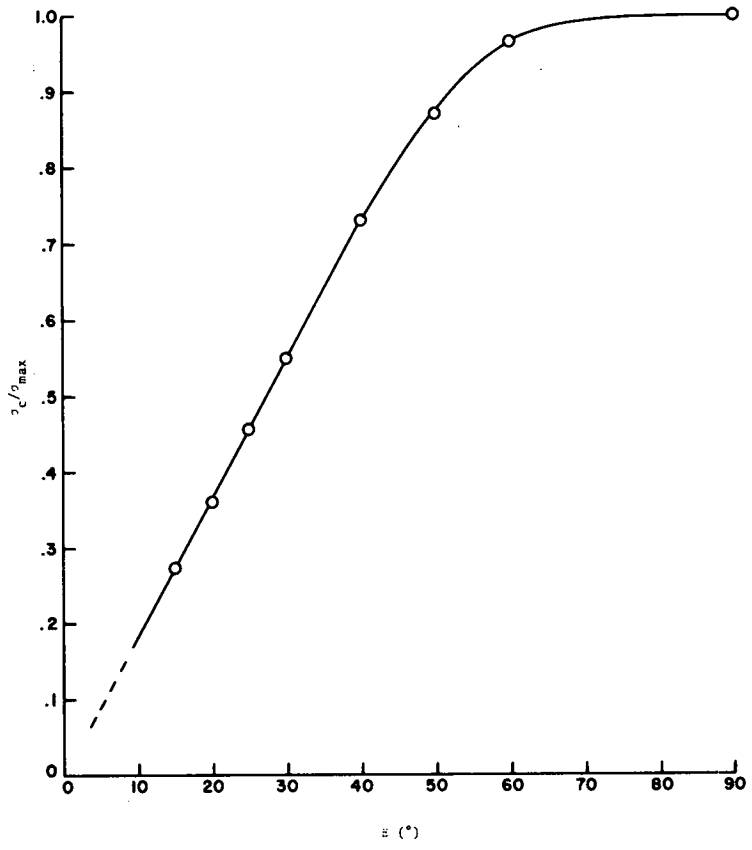

FIGURE 30 - Variation of normalized surface stress σ_c with cone angle

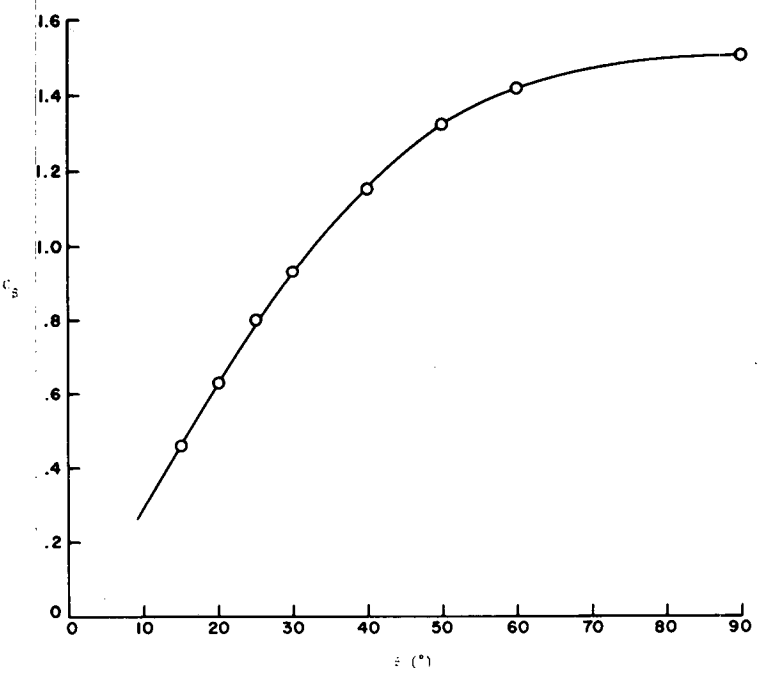

FIGURE 31 - Variation of drag coefficient C_β with cone angle

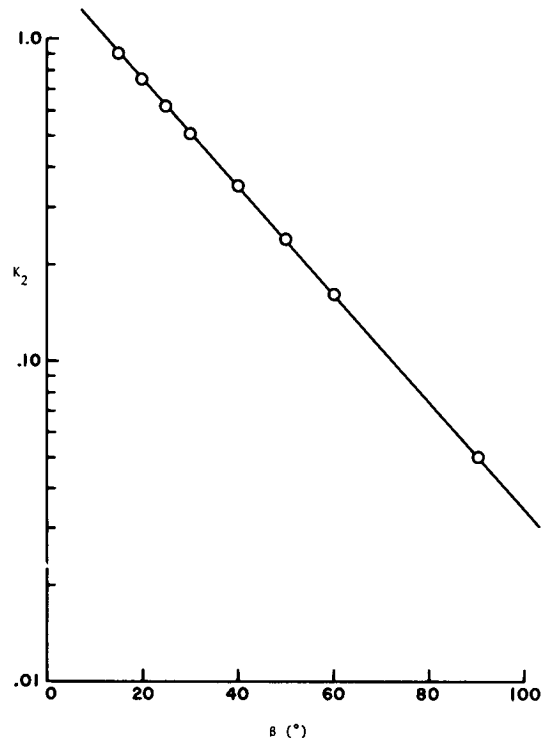

FIGURE 32 - Variation of stress exponent K_2 with cone angle

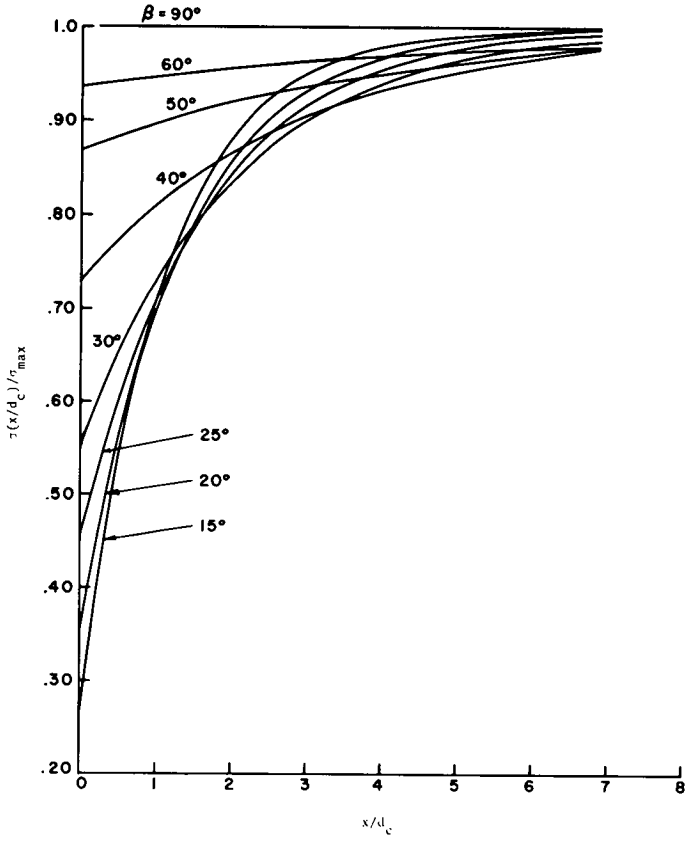

FIGURE 33 - Variation of stress with depth; various cone angles

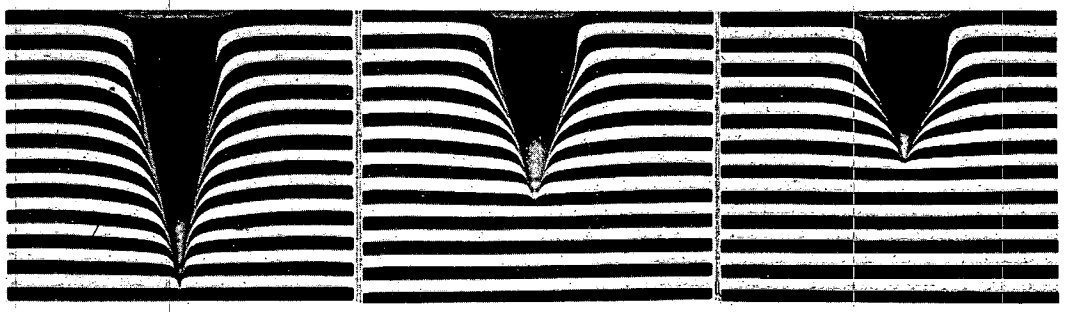

β = 10 β = 15 β = 20

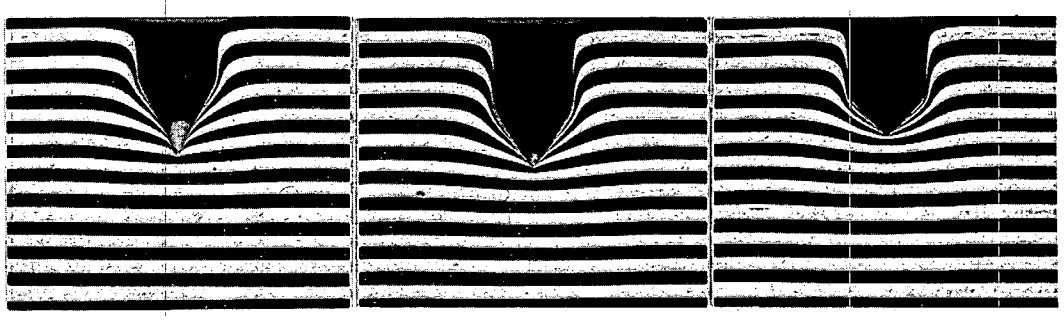

β = 25 β = 30 β = 40

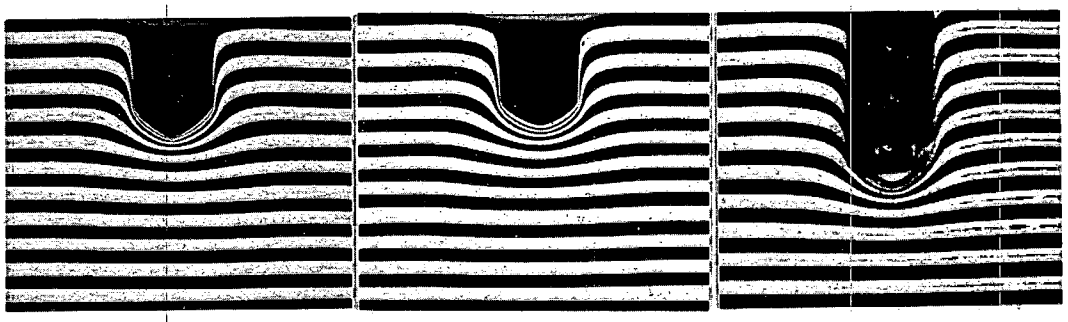

β = 50 β = 60 β = 90

FIGURE 34 - Deformation fields for various cone angles. Quasi-static penetration into laminated clay.

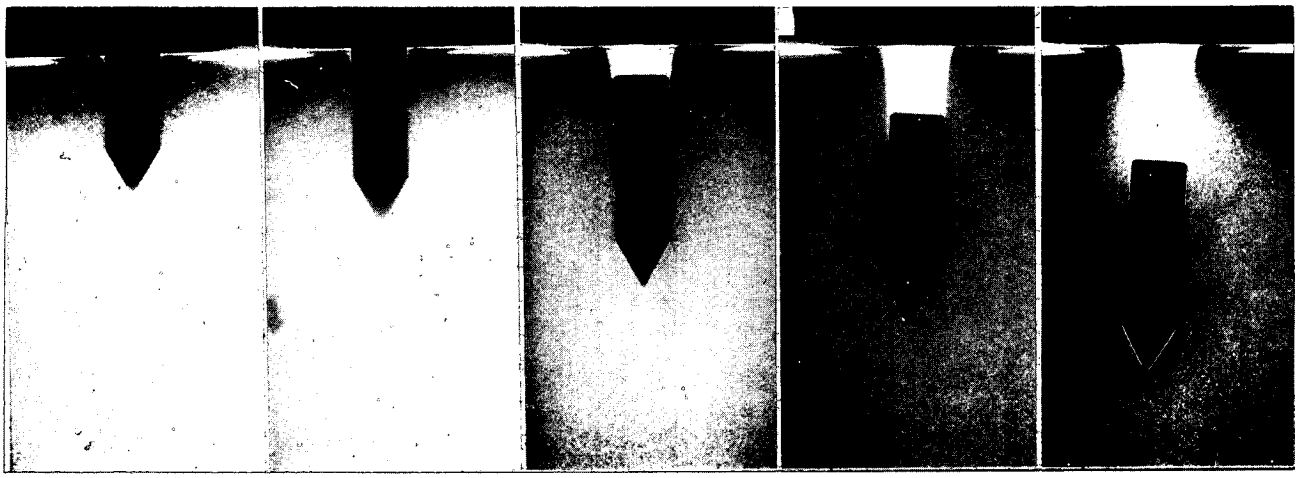

1653 ft/s 1930 ft/s 2418 ft/s 2674 ft/s 2985 ft/s

FIGURE 35 - Craters produced by 582 grain singly tapered WC projectiles, $\beta = 30°$. Various velocities.
Target, steel type 2

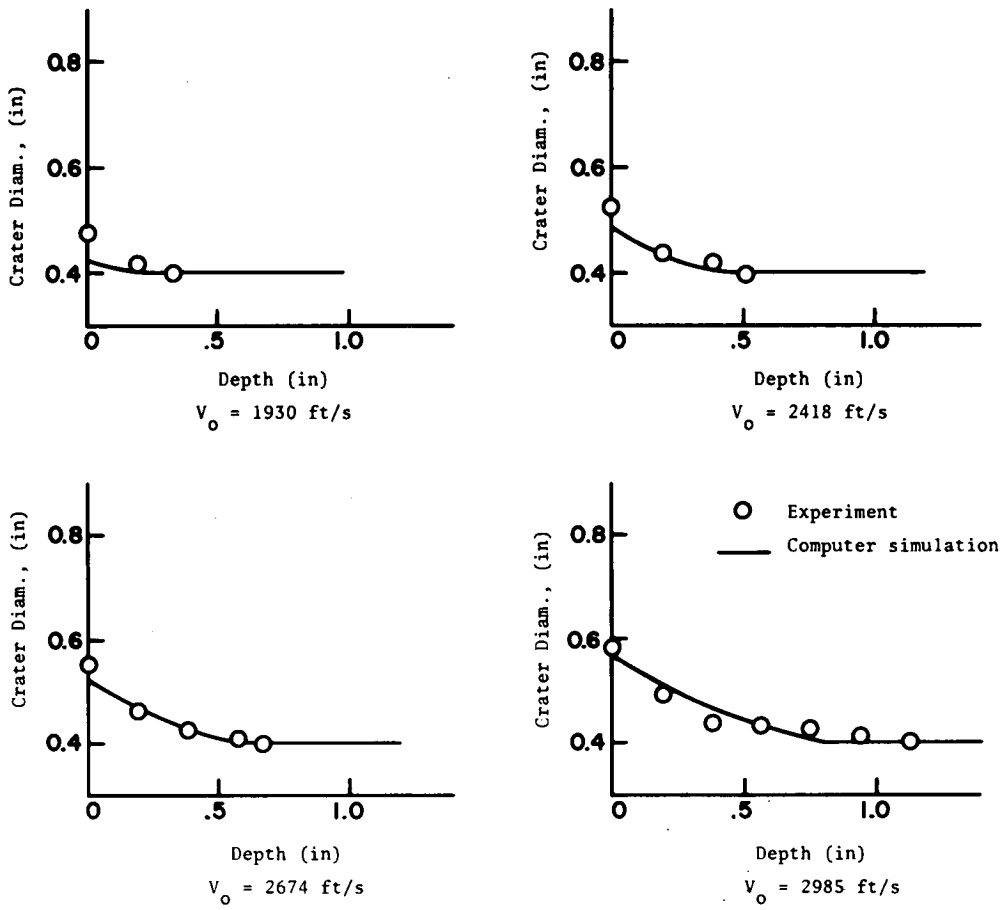

FIGURE 36 - Computer simulations for 582 grain singly tapered WC projectiles, $\beta = 30°$. Various velocities.
Target, steel type 2

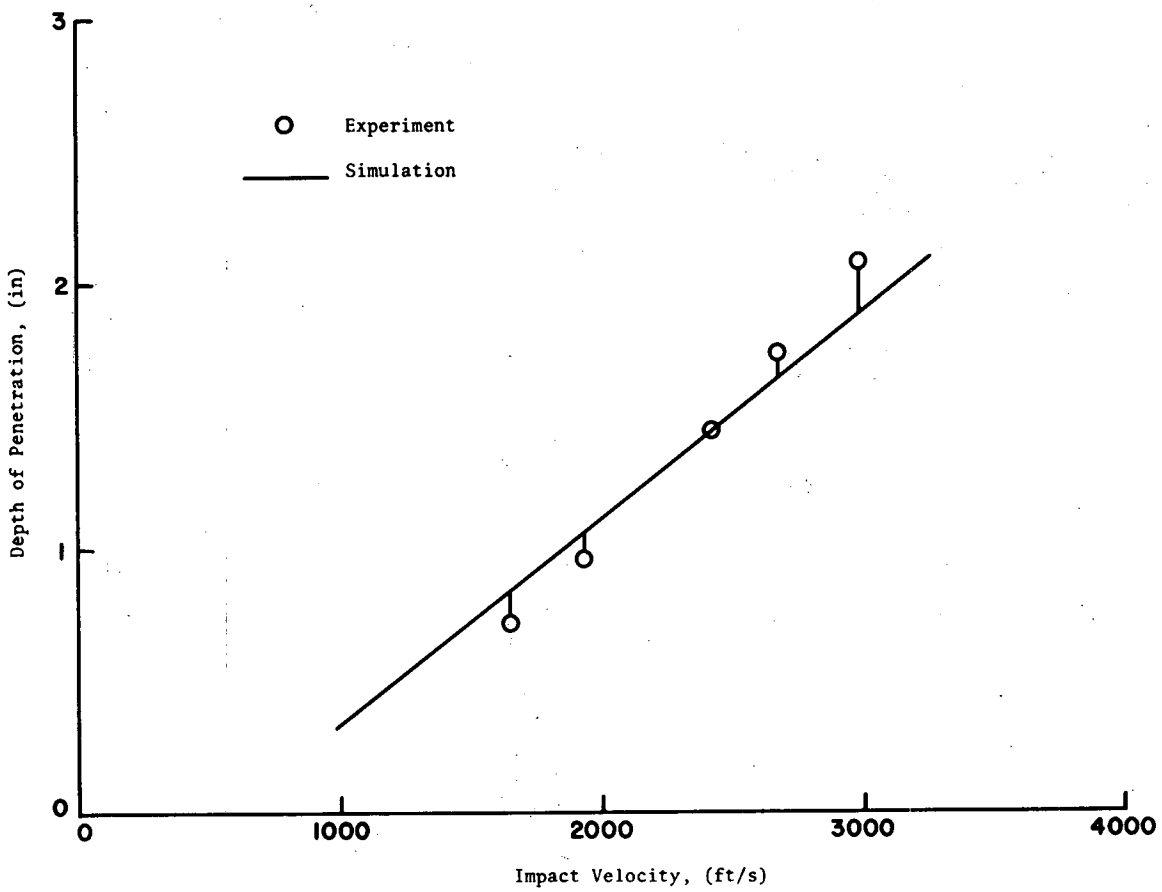

FIGURE 37 - Variation of penetration with velocity for 582 grain singly tapered WC projectiles, $\beta = 30°$. Target, steel type 2

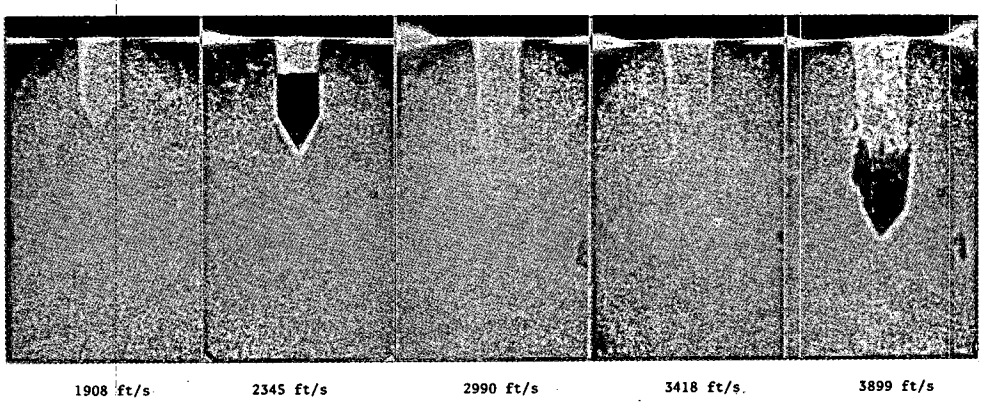

FIGURE 38 - Craters produced by 582 grain singly tapered WC projectiles, $\beta = 30°$. Various velocities.
Target, steel type 3

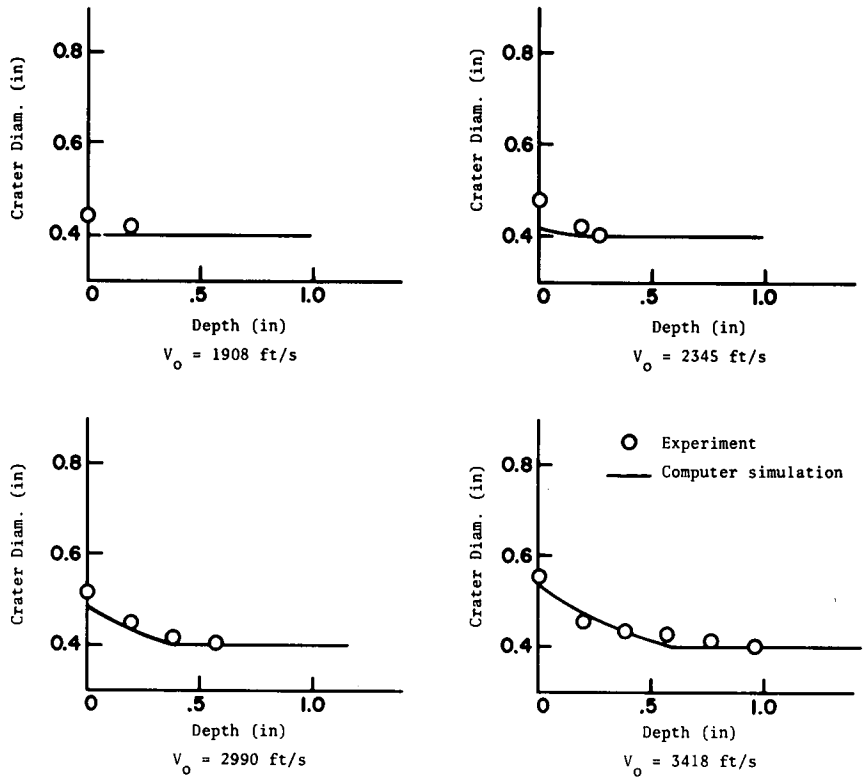

FIGURE 39 - Computer simulations for 582 grain singly tapered WC projectiles, $\beta = 30°$. Various velocities.
Target, steel type 3

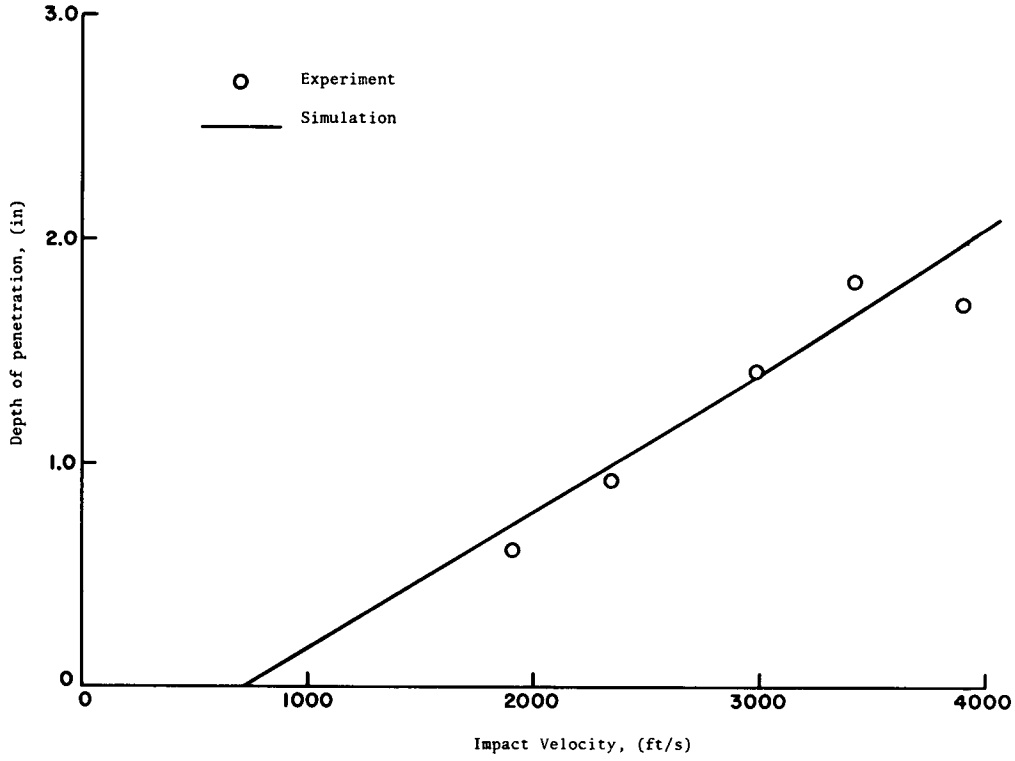

FIGURE 40 - Variation of penetration with velocity for 582 grain singly tapered WC projectiles, $\beta = 30°$. Target, steel type 3

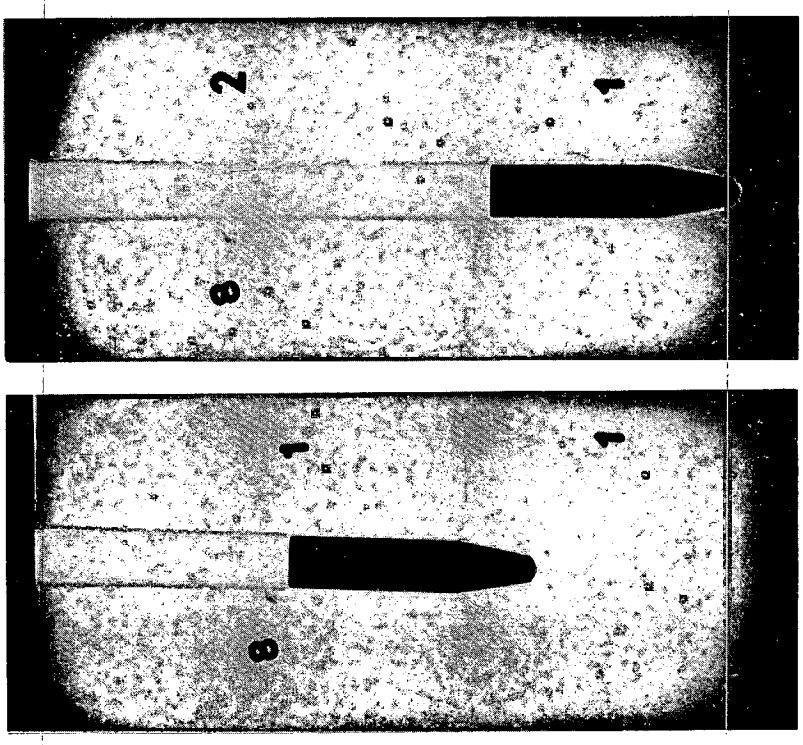

FIGURE 41 - Craters produced by 398 grain doubly tapered steel projectile; $\beta_1 = 60°$, $\beta_2 = 10°$; $d_t = 0.20$ inch. velocities, 2481 and 2004 ft/s. Target, aluminum type 1

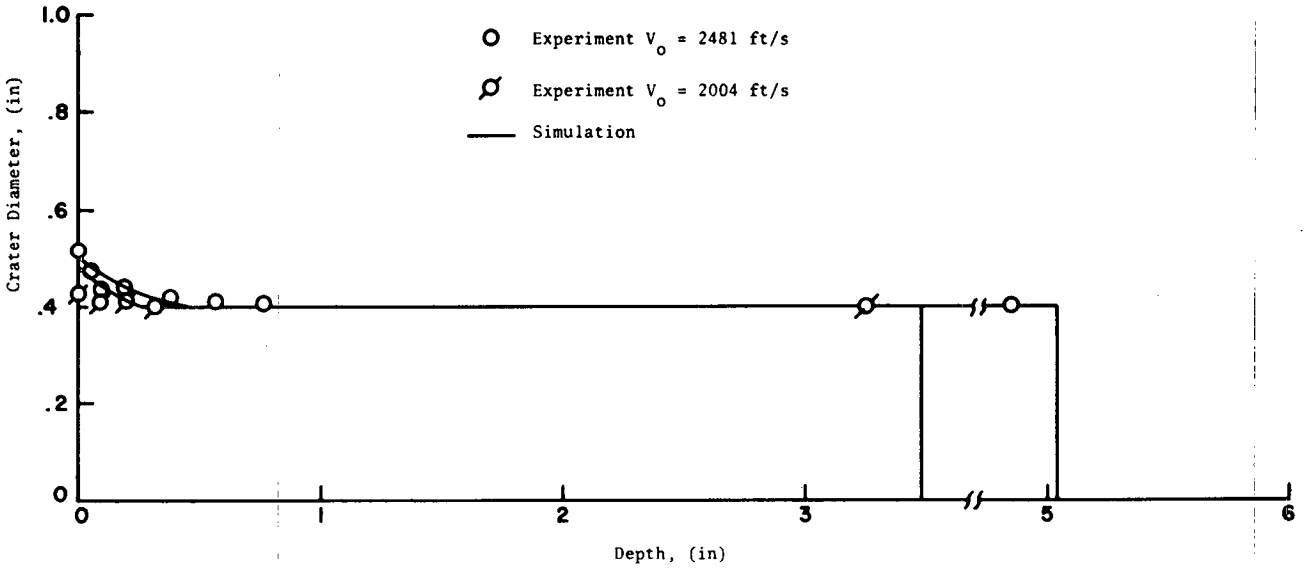

FIGURE 42 - Computer simulations for 398 grain doubly tapered steel projectile, $\beta_1 = 60°$, $\beta_2 = 10°$, $d_t = 0.20$ inch. velocities, 2481 and 2004 ft/s. Target, aluminum type 1

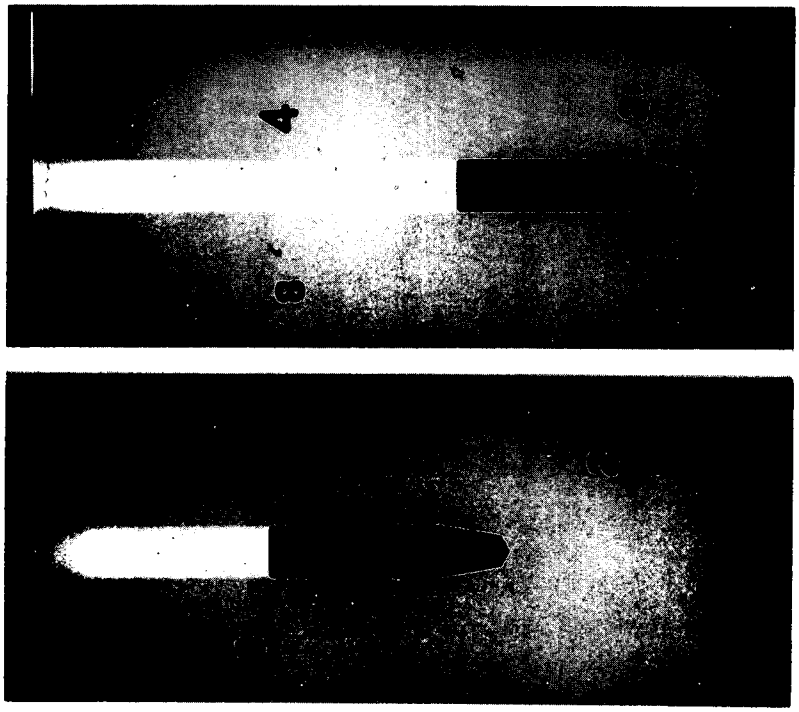

FIGURE 43 - Craters produced by 398 grain doubly tapered steel projectile; $\beta_1 = 60°$, $\beta_2 = 10°$; $d_t = 0.24$ inch. velocities, 2475 and 2016 ft/s. Target, aluminum type 1

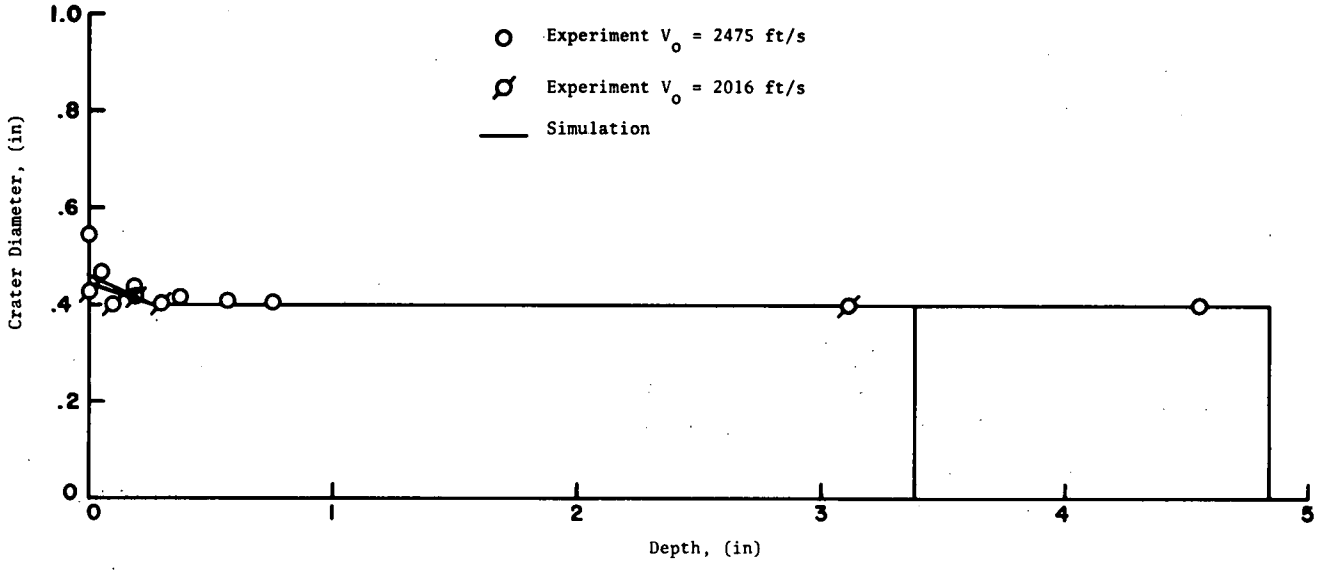

FIGURE 44 - Computer simulations for 398 grain doubly tapered steel projectile, $\beta_1 = 60°$, $\beta_2 = 10°$; $d_t = 0.24$ inch. velocities, 2475 and 2016 ft/s. Target, aluminum type 1

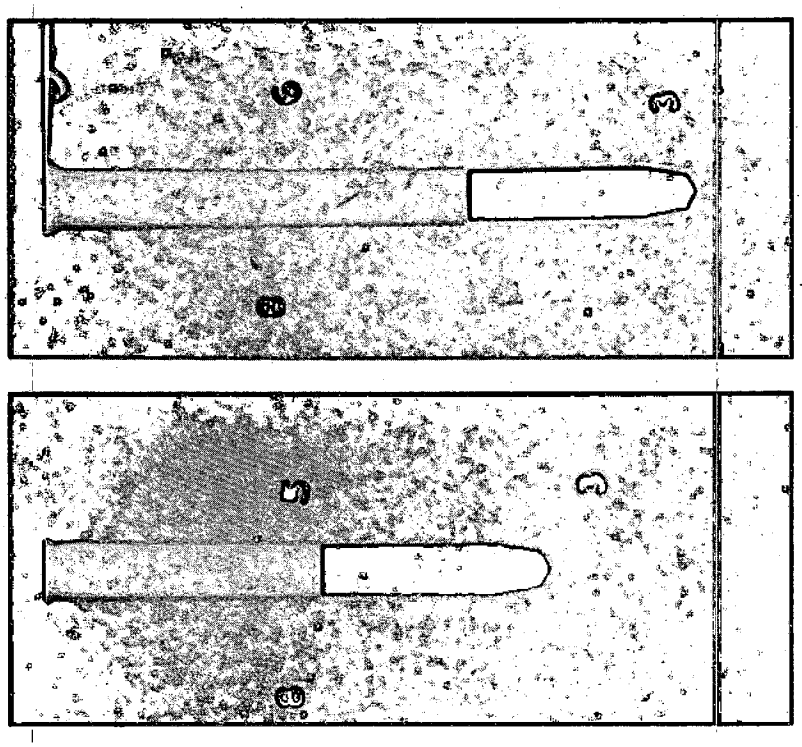

FIGURE 45 - Craters produced by 398 grain doubly tapered steel projectile; $\beta_1 = 60°$, $\beta_2 = 10°$; $d_t = 0.28$ inch. velocities, 2575 and 2200 ft/s. Target, aluminum type 1

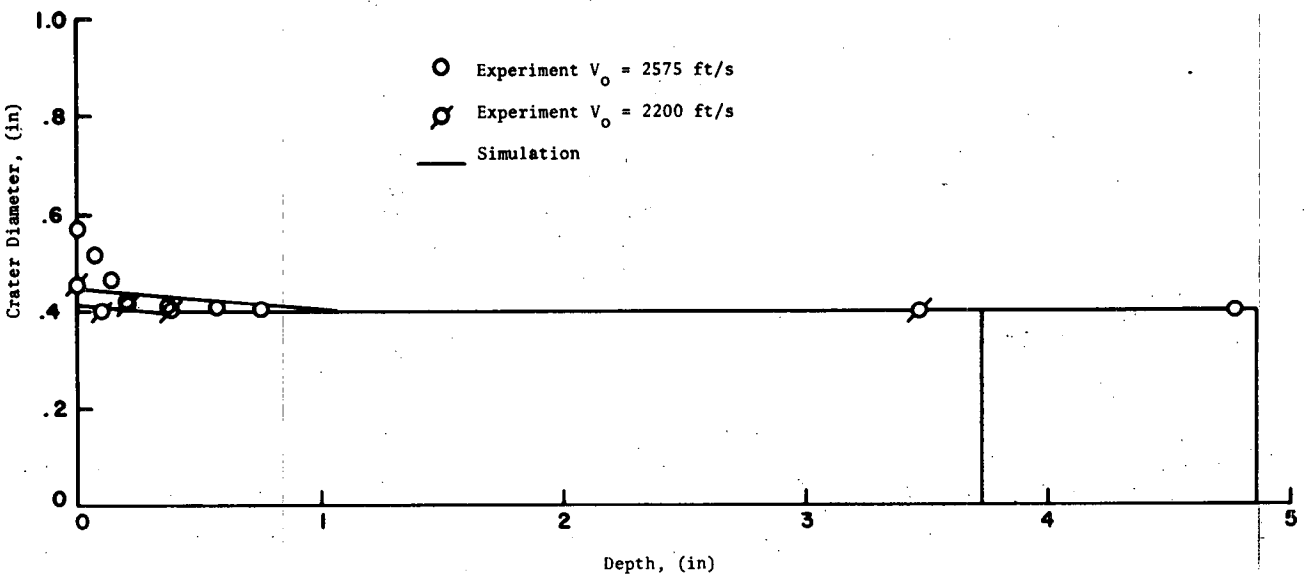

FIGURE 46 - Computer simulations for 398 grain doubly tapered steel projectile, $\beta_1 = 60°$, $\beta_2 = 10°$, $d_t = 0.28$ inch. velocities, 2575 and 2200 ft/s. Target, aluminum type 1

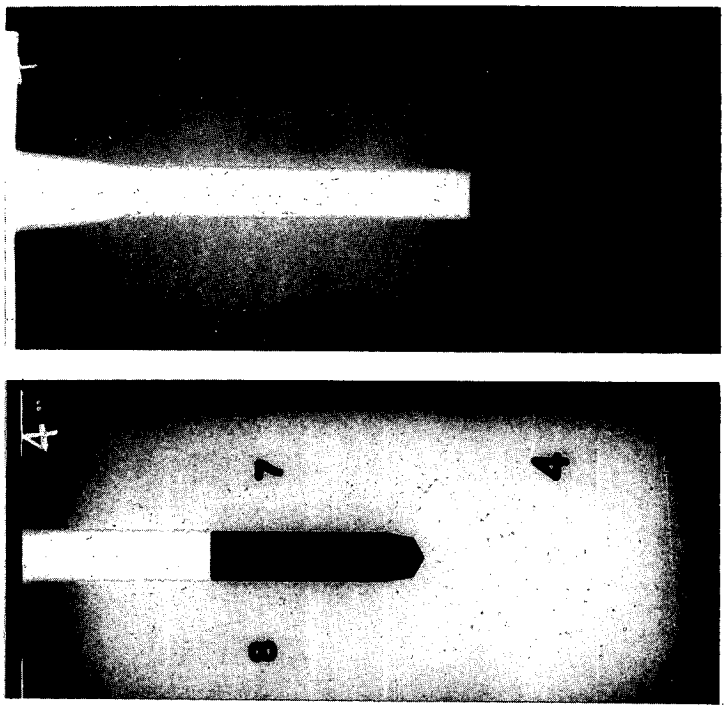

FIGURE 47 - Craters produced by 398 grain doubly tapered steel projectile; $\beta_1 = 60°$, $\beta_2 = 10°$; $d_t = 0.32$ inch. velocities, 2829 and 2070 ft/s. Target, aluminum type 1

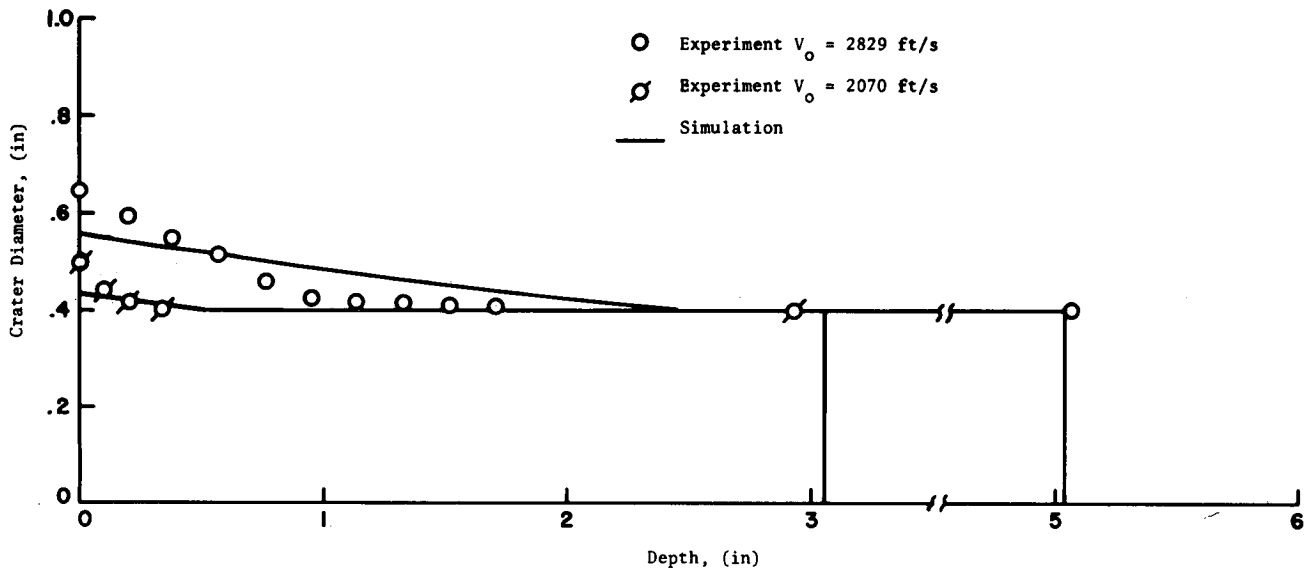

FIGURE 48 - Computer simulations for 398 grain doubly tapered steel projectile, $\beta_1 = 60°$, $\beta_2 = 10°$, $d_t = 0.32$ inch. velocities 2829 and 2070 ft/s. Target, aluminum type 1

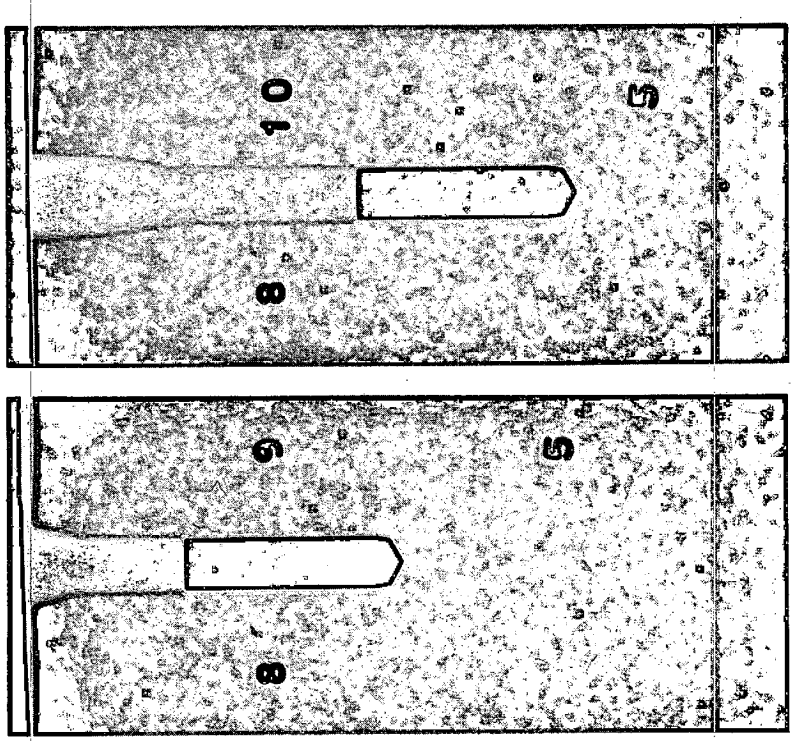

FIGURE 49 - Craters produced by 398 grain doubly tapered steel projectile; $\beta_1 = 60°$, $\beta_2 = 10°$; $d_t = 0.36$ inch. velocities, 2574 and 2018 ft/s. Target, aluminum type 1

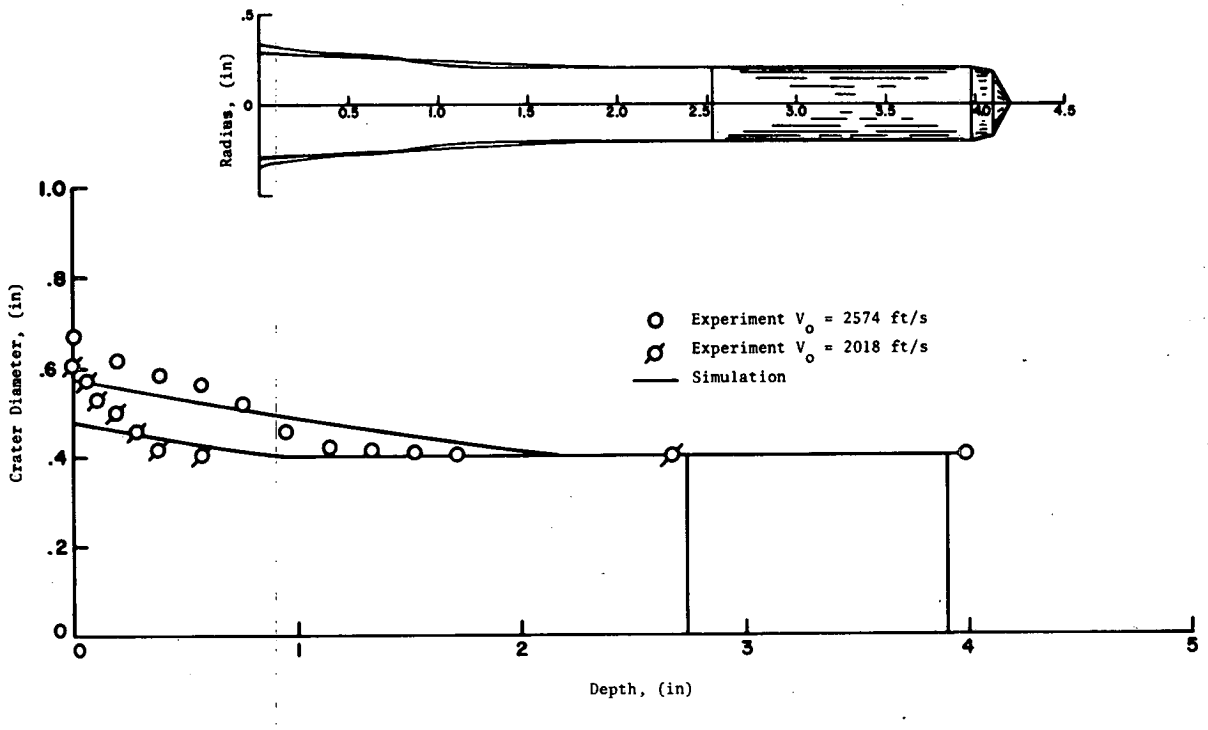

FIGURE 50 - Computer simulations for 398 grain doubly tapered steel projectile, $\beta_1 = 60°$, $\beta_2 = 10°$, $d_t = 0.36$ inch. velocities, 2574 and 2018 ft/s. Target, aluminum type 1

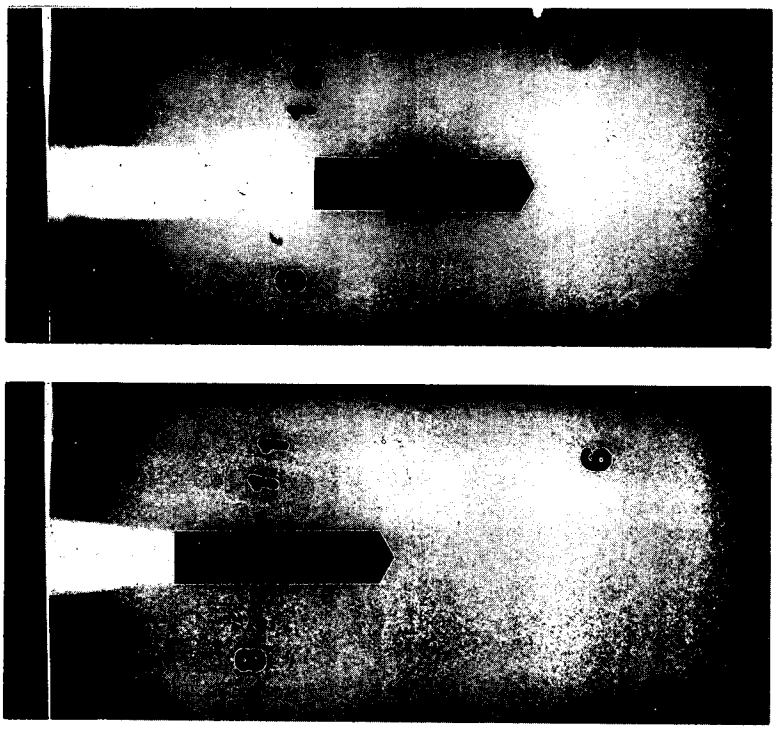

FIGURE 51 - Craters produced by 398 grain doubly tapered steel projectile; $\beta_1 = 60°$, $\beta_2 = 10°$; $d_t = .40$ inch. velocities, 2512 and 2010 ft/s. Target, aluminum type 1

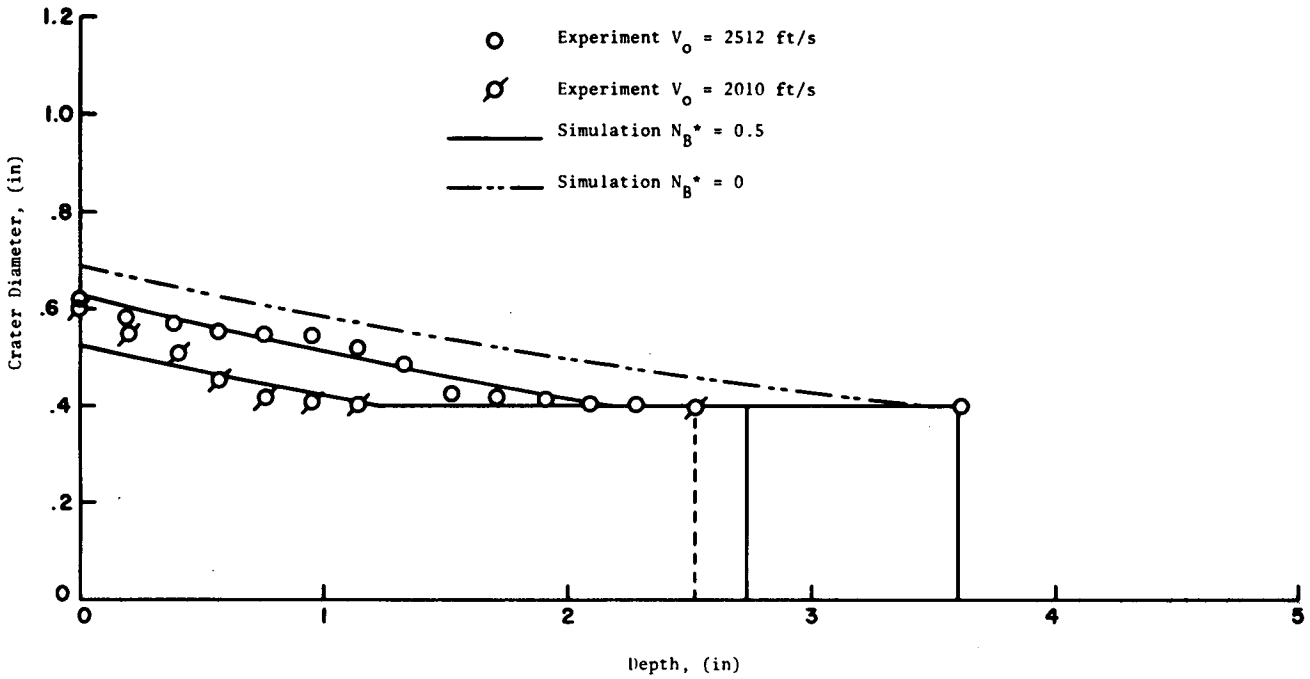

FIGURE 52 - Computer simulations for 398 grain doubly tapered steel projectile, $\beta_1 = 60°$, $\beta_2 = 10°$; d_t .40 inch. velocities, 2512 and 2010 ft/s. Target, aluminum type 1

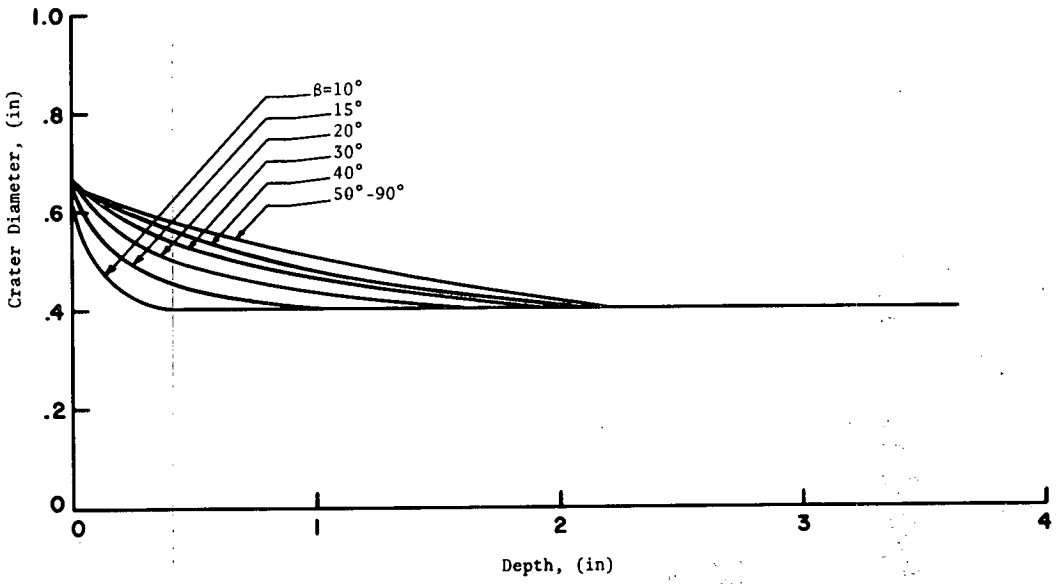

FIGURE 53 - Simulated crater profiles for 398 grain singly tapered steel projectiles, β = 10° to 90°, velocity, 2500 ft/s. Target aluminum type 1

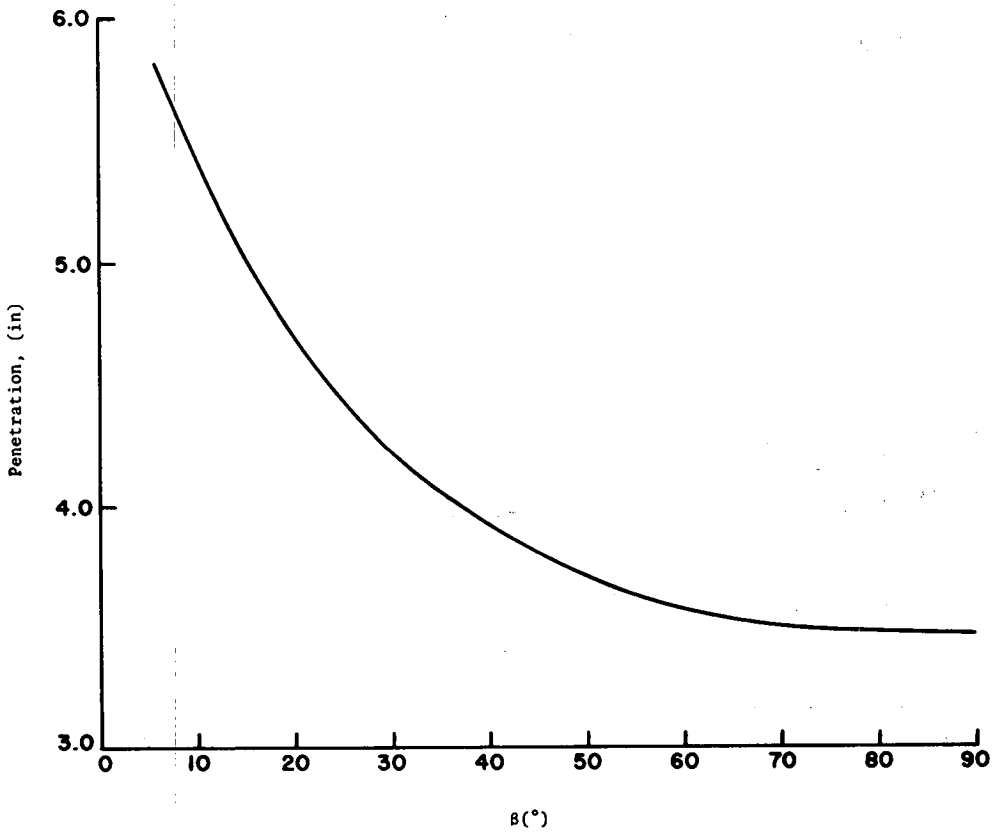

FIGURE 54 - Variation of maximum penetration with cone angle for 398 grain singly tapered steel projectiles. Velocity, 2500 ft/s. Target, aluminum type 1.

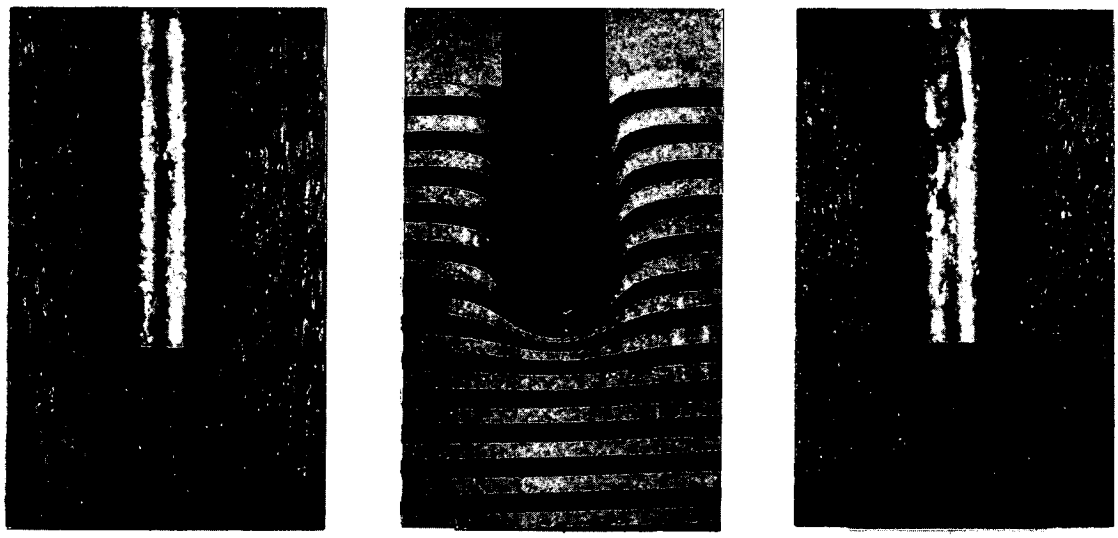

V_o = 2541 ft/s
Aluminum Target
β = 60°

V_o = 0.1 in/min
Clay Target
β = 90°

V_o = 2488 ft/s
Aluminum Target
β = 90°

FIGURE 55 - Comparison of static and dynamic deformation fields

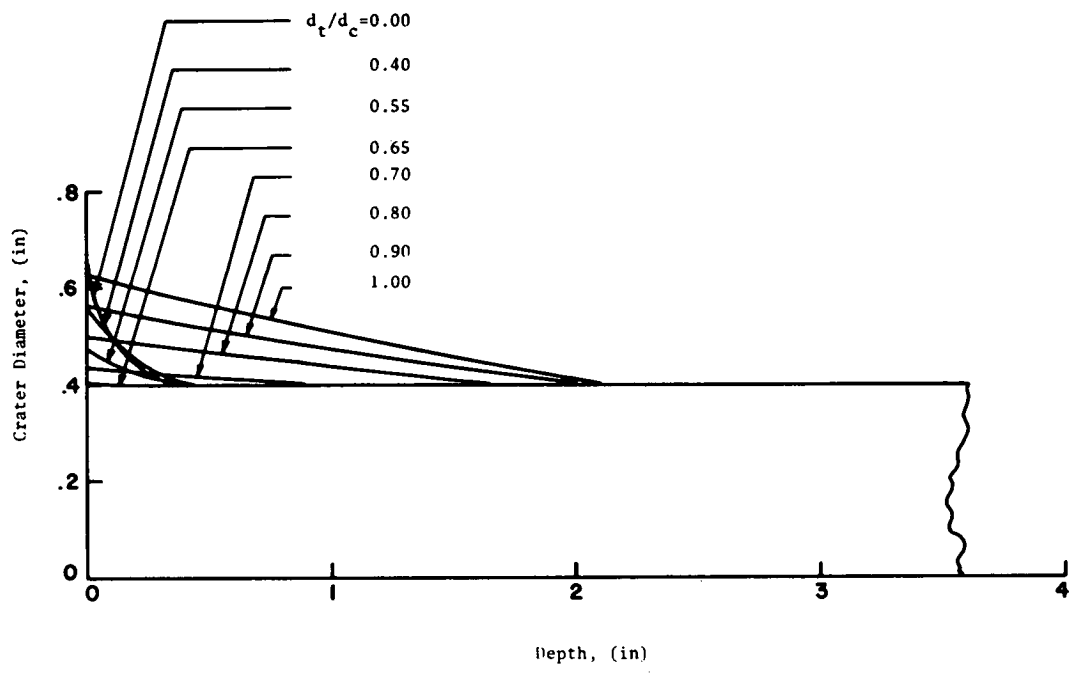

FIGURE 56 - Simulated crater profiles for 398 grain doubly tapered steel projectiles; β_1 = 60°, β_2 = 10°, d_t/d_c = 0 to 1.0. Velocity 2500 ft/s. Target, aluminum type 1

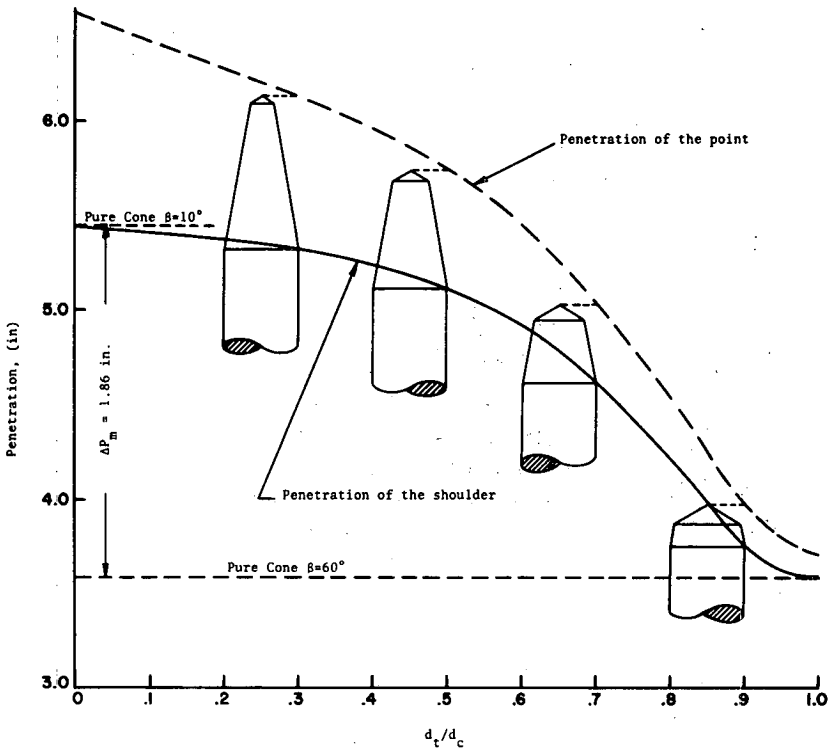

FIGURE 57 - Variation of maximum penetration with cone angle for 398 grain doubly tapered steel projectiles; $\beta = 60°$, $\beta_1 = 10°$, $d_t/d_c = 0$ to 1.0. Velocity 2500 ft/s. Target, aluminum type 1.

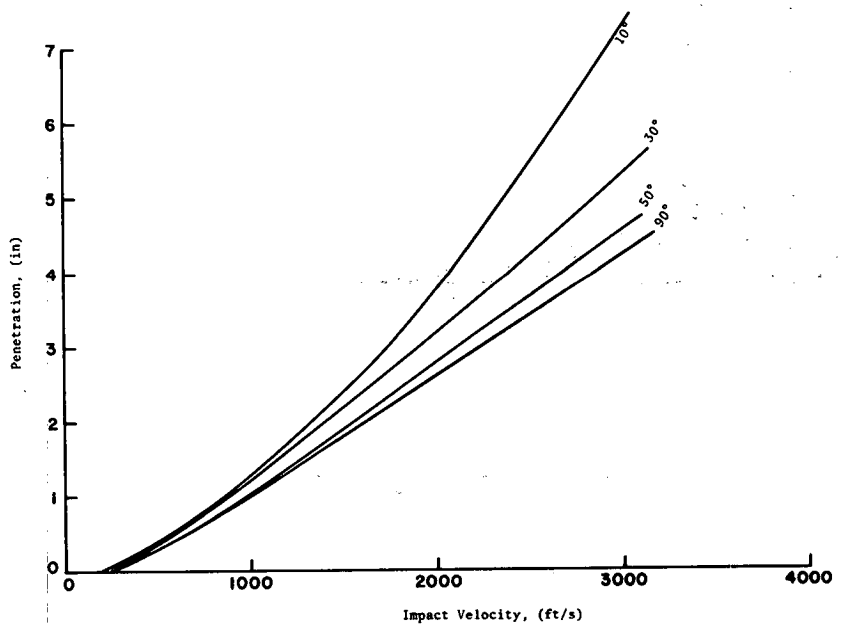

FIGURE 58 - Variation of penetration depth with velocity for 398 grain singly tapered steel projectile, $\beta = 30°$. Target aluminum type 1.

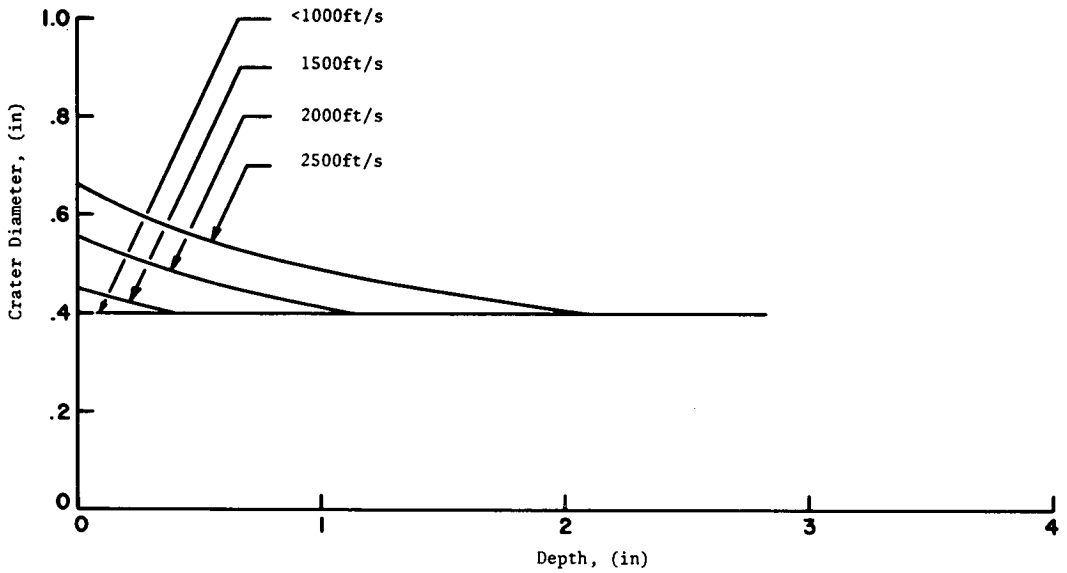

FIGURE 59 - Variation of crater profiles with velocity for 398 grain singly tapered steel projectile, $\beta = 30°$. Target, aluminum type 1.

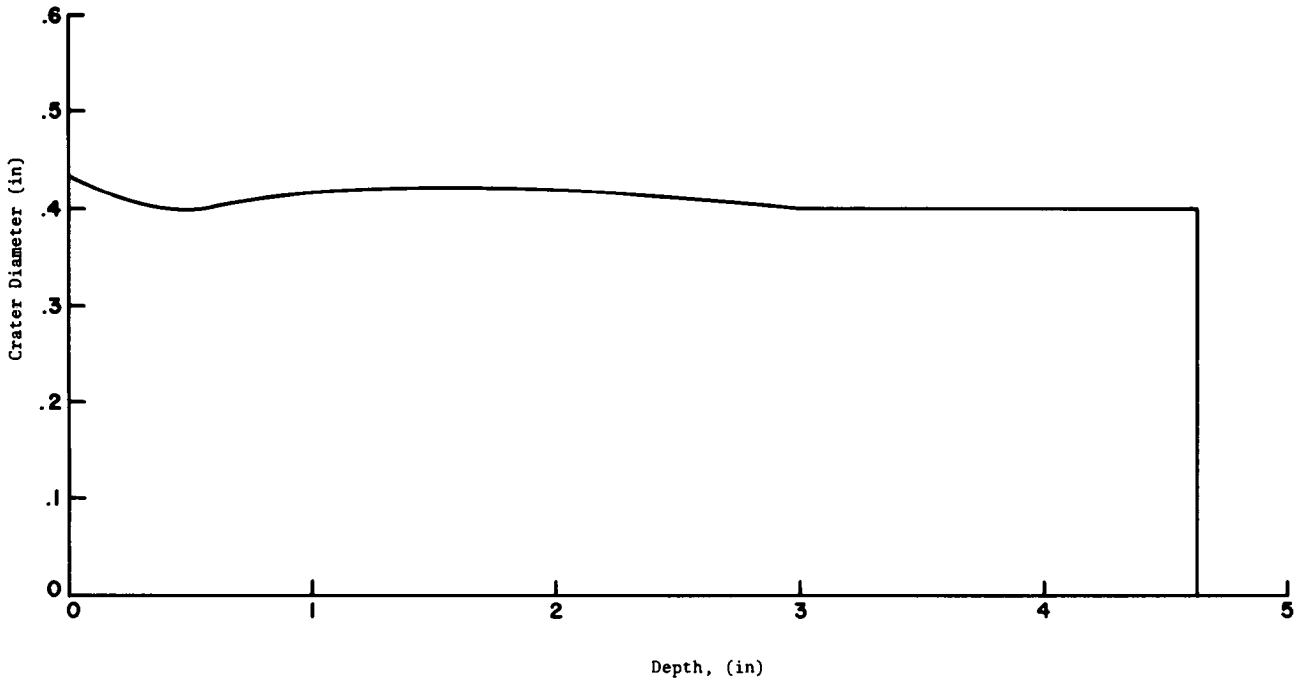

FIGURE 60 - Simulated profile showing secondary crater enlargement for 398 grain doubly tapered steel projectile, $\beta_1 = 40°$, $\beta_2 = 30°$, $d_t = .27$. Velocity = 2500 ft/s. Target, aluminum type 1.

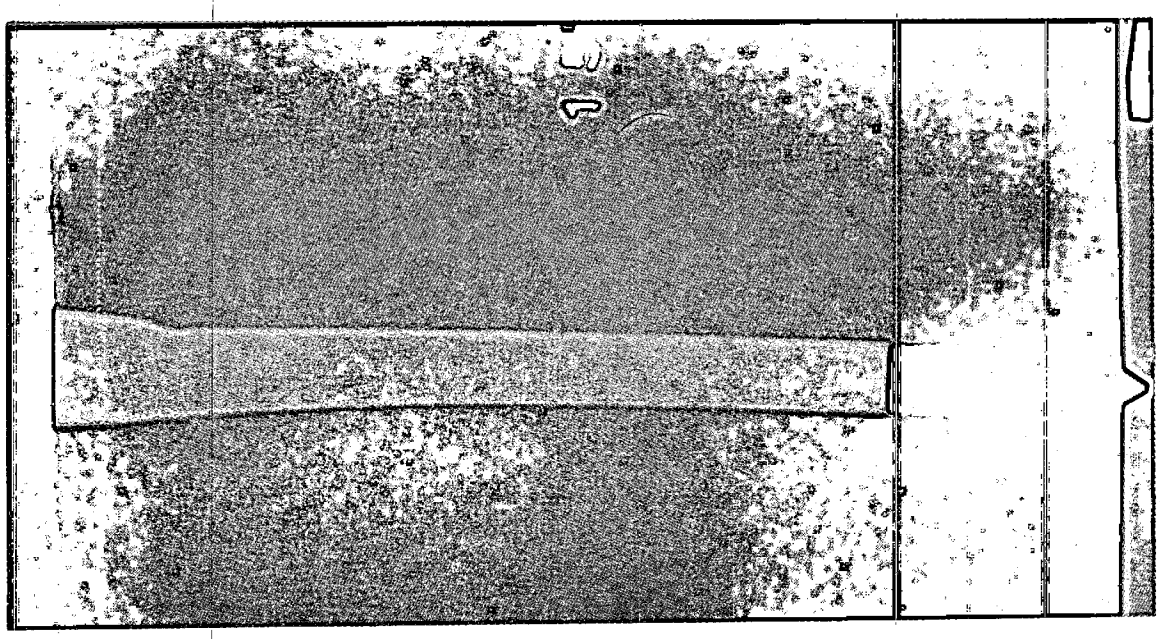

FIGURE 61 - Crater produced by 582 grain singly tapered WC projectile, $\beta = 30°$; velocity 2454 ft/s. Target, aluminum type 1

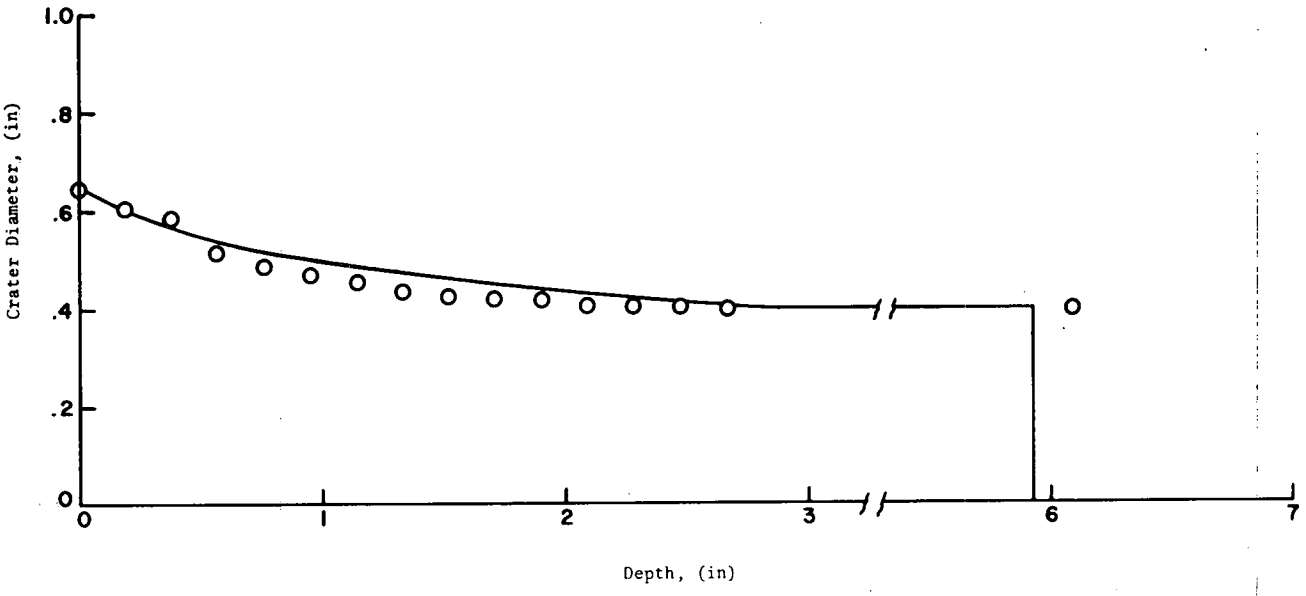

FIGURE 62 - Simulated profile for 582 grain singly tapered WC projectile, $\beta = 30°$, velocity 2454 ft/s. Target, aluminum type 1.

APPENDIX A

Computer Simulation 'AHAC'

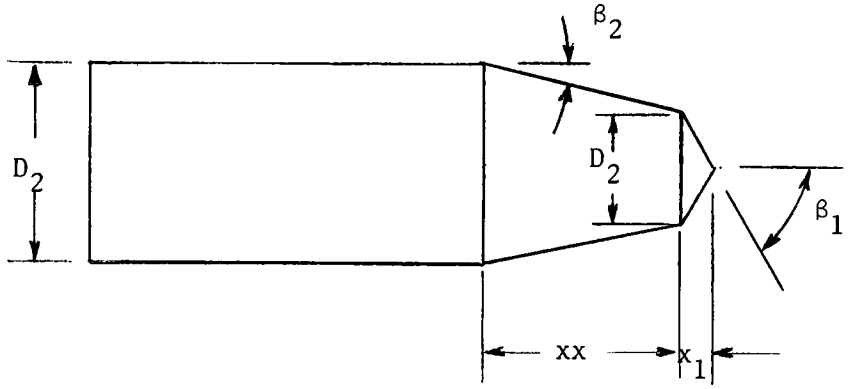

FIGURE A-1

The following equations (taken from the main text), have been programmed in APL to give a numerical solution for projectiles of the type shown in Figure A-1. The program is branched to handle the following cases:

i Singly-tapered cones, ($D_1 = D_2$)

ii Doubly-tapered cones:

a) Initial separation at the front shoulder produces crater enlargement greater than the diameter of the projectile body.

b) Separation at the front shoulder produces crater enlargement smaller than the diameter of the projectile body.

The starting velocity, i.e. the velocity corresponding to total immersion of the conical tip, is given by:

$$V_1 = (V_o^2 - (\pi d_1^3(\sigma_{c1})\text{Cot } \beta_1)/12\ M)^{\frac{1}{2}} \qquad \text{A-1}$$

Equation A-1 applies to all cases.

For Cases i and ii a,

The variation of target stress is:

$$\sigma_1(x) = \sigma_{max}(1-(1-\sigma_{c1}/\sigma_{max})\exp-(K_{2_1}\ X/D_1) \qquad \text{A-2}$$

The velocity decrement at depth x is:

$$\Delta V(x) = -A_1\Delta x(\sigma_1(x) + \tfrac{1}{2}\rho C_{\beta 1}V^2(x))/MV(x) \qquad \text{A-3}$$

The ballistic number is:

$$N_{B1} = \tfrac{1}{2}\rho V^2(x)/\sigma_1(x)$$

The crater area at depth x is:

$$A_H(x) = A_1(1 + N_{B1}\ C_{\beta 1} - N_B^*),\ N_{B1}\ C_{\beta 1} > N_B^* \qquad \text{A-4}$$
$$A_H(x) = A_1 \qquad ,\ N_{B1}\ C_{\beta 1} < N_B^*$$

For Case ii b

The variation in target stress is:

$$\sigma_1(x) = \sigma_{max}(1-(1 - \sigma_{c1}/\sigma_{max})\exp - (K_{21}(X - XX)/D_1)) \qquad \text{A-5}$$
$$\sigma_2(x) = \sigma_{max}(1-(1 - \sigma_{c2}/\sigma_{max})\exp - (K_{22}\ x/D_2))$$

The velocity decrement at depth x is:

$$\Delta V(x) = -\Delta X\Big\{A_1\sigma_1(x)(1 + N_{B1}C_{\beta 1}) - A_1\sigma_2(x)(1 + N_{B1}C_{\beta 1} - N_B^*)(1 + N_{B2}C_{\beta 2}) + A_2\sigma_2(x)(1 + N_{B2}C_{\beta 2})\Big\}/MV(x) \qquad \text{A-6}$$

The ballistic numbers are:

$$N_{B1} = \tfrac{1}{2}\ \sigma V^2(x)\sigma_1(x) \qquad \text{A-7}$$
$$N_{B2} = \tfrac{1}{2}\ \sigma V^2(x)\sigma_2(x)$$

The crater area at depth x, for $N_{B2}C_{\beta 2} > N_B^*$, is:

$$A_H(x) = A_2(1 + N_{B2}C_{\beta 2} - N_B^*) - A_1(1 + N_{B1}C_{\beta 1} - N_B^*)(N_{B2}C_{\beta 2} - N_B^*) \qquad \text{A-8}$$

The program is terminated when V(x) becomes negative. The size of the last increment Δx required to bring the velocity exactly to zero is then determined by an interpolation based on a volume/energy proportionality involving the local value of $\sigma_2(x)$.

In the following pages, a listing is given of the required inputs indicating the symbol equivalence; the APL program, the matrix 'MCOEF' and a sample solution for a doubly-tapered projectile. The matrix 'MCOEF' contains the values of C_β, K_2 and σ_c/σ_{max} for values of β from 0 - 90° in increments of 10°. If intermediate angles are required, these can be inputted separately, or a new NCOEF can be constructed by using the coefficient curves, (Figures 30, 31 and 32).

Input Parameters

σ_{max}	= SMAX	- Characteristic target strength - lbs/in^2
β_1	= B1	- Semi-apical angle - front cone - deg.
β_2	= B2	- " " - rear cone - deg.
D_1	= D1	- Base diameter - front cone - body diameter - in.
D_2	= D2	- Base diameter - rear cone - body diameter - in.
W	= W	- Weight - grains
	PTYPE	- 'Type of projectile'
	TYPE	- 'Type of target'
ρ	= RHO	- Density of target material
Dx	= DX	- Finite displacement step
σ_{c1}	= SC1	- Flow stress at surface associated with cone of semi-apical angle B1
σ_{c2}	= SC2	- Flow stress at surface; associated with cone of semi-apical angle B2
$C_{\beta 1}$	= CB1	- Drag coefficient for semi-apical angle B1
$C_{\beta 2}$	= CB2	- " " " " " B2
K_{21}	= K21	- Stress exponent for semi-apical angle B1
K_{22}	= K22	- " " " " " B2
N_B^*	= NBC	- Critical ballistic number
V_o	= VO	- Impact velocity
	CMOEF	- Coefficient matrix - (see print-out).

Output Parameters

X	= X	- Displacement vector - in.
V	= V	- Velocity vector corresponding to X - kft/s
A_H	= AH	- Cross-section area of crater - in^2
A_H/A_C	= AHBYAC	- Ratio of crater area to projectile cross-section area.
D_H	= DH	- Crater diameter vector.

```
     ∇AHAC
[1]   'ENTER SMAX B1 B2 VO RHO W(GRAINS) PTYPE TYPE D1 D2'
[2]   L1←+/B1≥MCOEF[;1]
[3]   L2←+/B2≥MCOEF[;1]
[4]   ZZZ←JJ←KK←1
[5]   ' TARGET'
[6]   '-------'
[7]   TYPE;'     RHO ';RHO;' LB/CU IN '
[8]   'SMAX ';SMAX;' PSI'
[9]   'SC1  ';SC1←0 RND SMAX×MCOEF[L1;4];' PSI     SC2   ';SC2←0 RND SMAX×MCOEF[L2;4];' PSI'
[10]  'K21  ';K21←MCOEF[L1;3];'     K22   ';K22←MCOEF[L2;3]
[11]  'NBC  ';NBC←.5
[12]  ''
[13]  'PROJECTILE'
[14]  '----------'
[15]  PTYPE;'     VO ';VO;' FT/SEC       W ';W;' GRAINS'
[16]  ' 1   ';B1;' (∘)       B2   ';B2;' (∘)'
[17]  'CB1  ';CB1←MCOEF[L1;2];'    CB2  ';CB2←MCOEF[L2;2]
[18]  'D1   ';D1;' IN       D2;  ';D2;' IN'
[19]  'DX   ';DX
[20]  →ABC×⍳D1=D2
[21]  XX←(D2-D1)÷2×TAN B2
[22]  →ABD×D1≠D2
[23] ABC:XX←0
[24] ABD:VO←VO×12
[25]  RHO←RHO÷386.51
[26]  A2←○(D2*2)÷4
[27]  A1←○(D1*2)÷4
[28]  M←(1÷386.51)×W÷7000
[29]  NBC←(RHO×VO*2)÷2×SC1
[30]  X1←D1÷2×TAN B1
[31]  V1←VN←V←((VO*2)-(○SC1×(D1-2)×X1÷6×M))*.5
[32]  N1←.5×RHO×CB1
[33]  N2←.5×RHO×CB2
[34]  XN←X←DH←AHB←AC←0
[35]  NB1←NB←(RHO×V*2)÷2×SC1
[36]  AH←A1×1÷(NB×CB1)-NBC
[37]  AH←(AH×(NB×CB1)≥NBC)+A1×(NB×CB1)<NBC
[38]  ' DISPL.          VELOCITY          HOLE AREA          AH/AC          HOLE DIA.
[39]  '  IN.            FPT/SEC            SQ IN                          IN'
[40] AREA12:→AREA8×⍳(AH<A2)
[41] AREA2:S1←SMAX×(1-(1-SC1÷SMAX)××-K21×(XN+DX÷2)÷D1)
[42]  DV←-(S1+N1×(VN-2))×A1×DX÷M×VN
[43]  V←V,VN←VN+DV
[44]  X←X,XN←XN+DX
[45]  NBN1←(RHO×VN*2)÷2×S1
[46]  →AREA4×⍳((NBN1×CB1)≤NBC)×(A1=A2)
[47]  AHN←A1×1 (NBN1×CB1)-NBC
[48]  →AREA9×⍳AHN<A2
[49]  AH←AH,AHN
[50]  →AREA5
```

```
[51] AREA4:AH←AH,AHN←A2
[52] AREA5:→AREA2×⍳VN>0
[53] AREA3:AHBYAC←AH÷A2
[54]  DH←(4×AH÷○1)*.5
[55]  MAT←⍉(5,⍴V)⍴3 RND X,(V÷12000),AH,AHBYAC,DH
[56]  VO←VO÷12
[57]  RHO←RHO×386.51
[58]  MAT
[59]  XC←X[(⍴X)-1]+(DX×(V[(⍴V)-1]÷V[(⍴V)-1]-V[⍴V]))+(XX×KK=0)-XX×JJ=0
[60]  XM←XC+X1 XX×JJ=0
[61]  'MAX PENETRATION...';3 RND XM;' IN. MEASURED FROM THE POINT'
[62]  'TOTAL NOSE LENGTH IS  ';3 RND X1+XX
[63]  'CYLINDRICAL PENETRATION IS ';3 RND XC
[64]  'HOLE DIAMETERS CORESPOND TO DISPL. FROM SURFACE'
[65]  →AREA13×⍳(ZZZ=0)
[66]  'INITIAL SEPARATION AT THE FRONT SHOULDER'
[67]  →0
[68] AREA13:'INITIAL SEPARATION IS AT THE REAR SHOULDER'
[69]  →0
[70] AREA8:ZZZ←X←KK←JJ←0
[71]  VOLC←○(D1*3)÷24×TAN B1
[72]  RH←(AH÷○1)*.5
[73]  H1←(RH-R1←D1÷2)÷TAN B2
[74]  VOLB←(○H1÷3)×((R1*2)+(R1×RH)+RH*2)
[75]  R2←D2÷2
[76]  H2←(R2-RH)÷TAN B2
[77]  VOLA←(○H2÷3)×((R2*2)+(R2×RH)+RH*2)
[78]  DELE←(SC1×(VOLB+VOLC))+SC2×VOLA
[79]  V←VN←V1←((VO*2) 2×DELE÷M)*.5
[80]  NBN1←NB1←(RHO×V1*2)÷2×SC1
[81]  NBN2←NB1×SC1÷SC2
[82]  AH←(A2×1-NBC-NBN2×CB2)-A1×(1-NBC-NBN1×CB1)×(NBN2×CB2)-NBC
[83] AREA1:S1←SMAX×(1-(1-SC1÷SMAX)×*-K21×((XN XX×KK=0)+DX÷2)÷D1)
[84]  S2←SMAX×(1-(1-SC2÷SMAX)×* K22×((XN-XX×KK=1)+DX÷2)÷D2)
[85]  NBN1←(RHO×VN*2)÷2×S1
[86]  NBN2←NBN1×S1÷S2
[87]  DV←-(DX÷M×VN)×(A1×S1×1 NBN1×CB1)+(A2×S2×1+NBN2×CB2) (A1×S2×(1-NBC-NBN1×CB1)×1+NBN2×CB2)
[88]  V←V,VN←VN+DV
[89]  X←X,XN←XN+DX
[90]  →AREA6×⍳((NBN2×CB2)≤NBC)
[91]  →AREA10
[92] AREA9:JJ←0
[93]  X←¯1↓X
[94]  XN←X[⍴X]
[95]  V←¯1↓V
[96]  VN←V[⍴V]
[97]  →AREA1
[98] AREA10:AH←AH,AHN←(A2×1-NBC-NBN2×CB2)-A1×(1 NBC-NBN1×CB1)×(NBN2×CB2)-NBC
[99]  →AREA7
[100]AREA6:AH←AH,AHN←A2
[101]AREA7:→AREA1×⍳VN>0
[102] →AREA3
[103] AH
      ∇
```

MCOEF

ANGLE	*CB*	*K2*	*SC/SMAX*
0	0	1.62	0
10	0.29	1.1	0.183
15	0.46	0.9	0.274
20	0.63	0.75	0.36
25	0.8	0.62	0.457
30	0.93	0.505	0.549
40	1.15	0.35	0.731
50	1.32	0.24	0.869
60	1.415	0.161	0.966
70	1.465	0.109	0.9 4
80	1.49	0.074	0.997
90	1.5	0.05	1

```
      AHAC
ENTER SMAX B1 B2 VO RHO W(GRAINS) PTYPE TYPE D1 D2
AHAC[2]
      →2
 TARGET
--------

ALUM TYPE 1      RHO 0.1 LB/CU IN
SMAX 87500 PSI
SC1  84500 PSI      SC2   31500 PSI
K21   0.161      K22   0.75
NRC   0.5

PROJECTILE
----------

D T CONE      VO 2000 FT/SEC       W 350 GRAINS
B1   60 (∘)       B2   20 (∘)
CB1  1.415     CB2  0.63
D1   0.35 IN       D2;  0.4 IN
DX   0.2
```

DISPL. IN.	VELOCITY KFT/SEC	HOLE AREA SQ IN	AH/AC	HOLE DIA. IN
0	1.993	0.167	1.331	0.461
0.2	1.895	0.156	1.239	0.445
0.4	1.797	0.145	1.15	0.429
0.6	1.699	0.134	1.067	0.413
0.8	1.606	0.126	1	0.4
1	1.507	0.126	1	0.4
1.2	1.399	0.126	1	0.4
1.4	1.282	0.126	1	0.4
1.6	1.152	0.126	1	0.4
1.8	1.008	0.126	1	0.4
2	0.842	0.126	1	0.4
2.2	0.645	0.126	1	0.4
2.4	0.389	0.126	1	0.4
2.6	0.03	0.126	1	0.4

```
MAX PENETRATION...2.687 IN. MEASURED FROM THE POINT
TOTAL NOSE LENGTH IS  0.17
CYLINDRICAL PENETRATION IS 2.517
HOLE DIAMETERS CORESPOND TO DISPL. FROM SURFACE
INITIAL SEPARATION AT THE FRONT SHOULDER
```